



NOVA

University of Newcastle Research Online

nova.newcastle.edu.au

Hu, Cheng; Tu, Shuchen; Tian, Na; Ma, Tianyi; Zhang, Yihe; Huang, Hongwei. "Photocatalysis Enhanced by External Fields". *Angewandte Chemie International Edition* Vol. 60, Issue 30, p. 16309-16328 (2021).

Available from: <http://dx.doi.org/10.1002/anie.202009518>

Hu, Cheng; Tu, Shuchen; Tian, Na; Ma, Tianyi; Zhang, Yihe; Huang, Hongwei. "Photocatalysis Enhanced by External Fields". *Angewandte Chemie International Edition* Vol. 60, Issue 30, p. 16309-16328 (2021), which has been published in final form at <http://dx.doi.org/10.1002/anie.202009518>.

This article may be used for non-commercial purposes in accordance with Wiley Terms and Conditions for Use of Self-Archived Versions. This article may not be enhanced, enriched or otherwise transformed into a derivative work, without express permission from Wiley or by statutory rights under applicable legislation. Copyright notices must not be removed, obscured or modified. The article must be linked to Wiley's version of record on Wiley Online Library and any embedding, framing or otherwise making available the article or pages thereof by third parties from platforms, services and websites other than Wiley Online Library must be prohibited.

Accessed from: <http://hdl.handle.net/1959.13/1475272>



Angewandte Chemie

Eine Zeitschrift der Gesellschaft Deutscher Chemiker

GDCh

www.angewandte.de

Akzeptierter Artikel

Titel: External fields enhanced photocatalysis

Autoren: Cheng Hu, Shuchen Tu, Na Tian, Tianyi Ma, Yihe Zhang, and Hongwei Huang

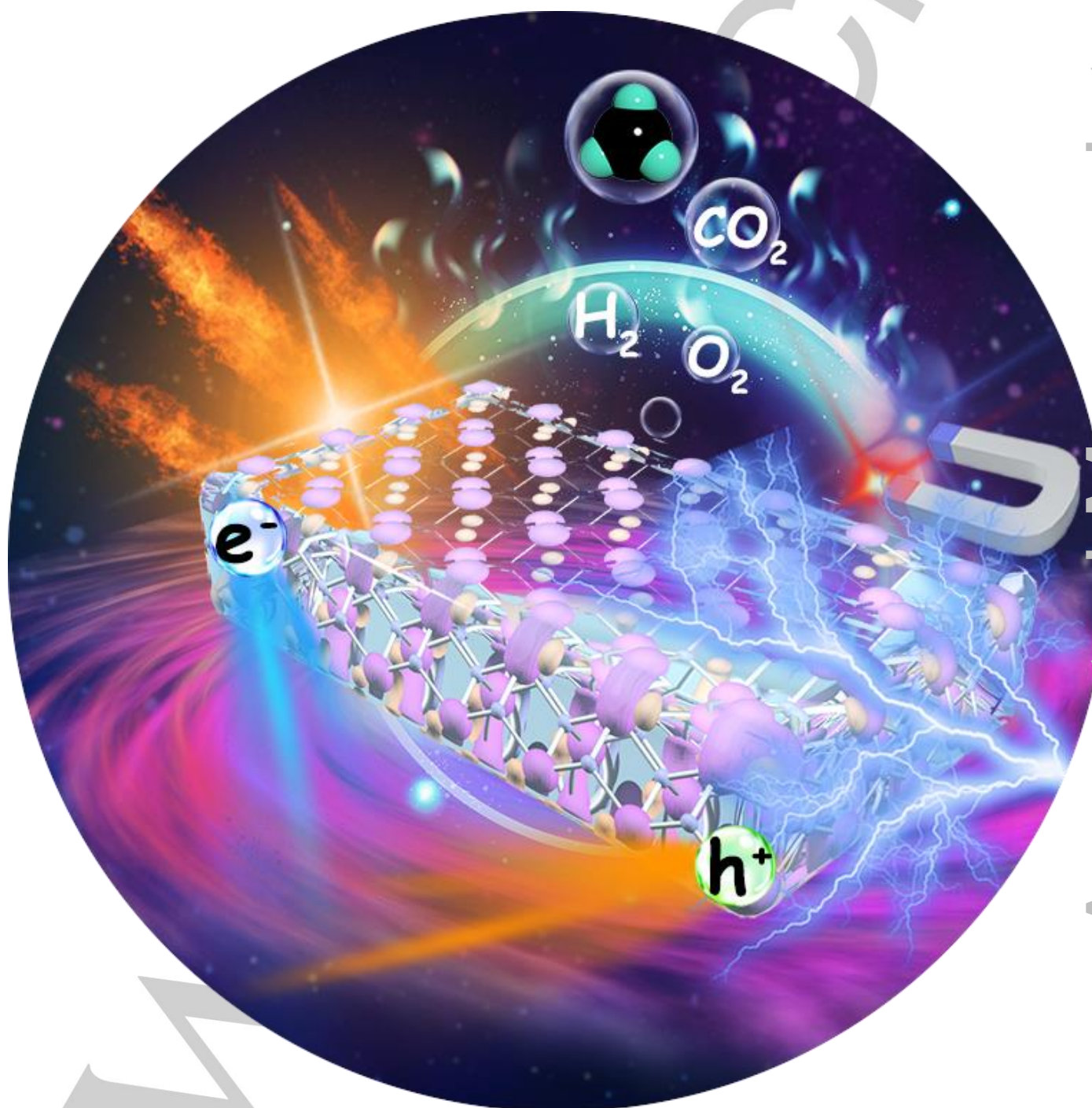
Dieser Beitrag wurde nach Begutachtung und Überarbeitung sofort als "akzeptierter Artikel" (Accepted Article; AA) publiziert und kann unter Angabe der unten stehenden Digitalobjekt-Identifizierungsnummer (DOI) zitiert werden. Die deutsche Übersetzung wird gemeinsam mit der endgültigen englischen Fassung erscheinen. Die endgültige englische Fassung (Version of Record) wird ehestmöglich nach dem Redigieren und einem Korrekturgang als Early-View-Beitrag erscheinen und kann sich naturgemäß von der AA-Fassung unterscheiden. Leser sollten daher die endgültige Fassung, sobald sie veröffentlicht ist, verwenden. Für die AA-Fassung trägt der Autor die alleinige Verantwortung.

Zitierweise: *Angew. Chem. Int. Ed.* 10.1002/anie.202009518

Link zur VoR: <https://doi.org/10.1002/anie.202009518>

External fields enhanced photocatalysis

Cheng Hu,^[a] Shuchen Tu,^[a] Na Tian,^{*[a]} Tianyi Ma,^{*[b]} Yihe Zhang,^[a] Hongwei Huang^{*[a]}



Accepted Manuscript

- [a] C. Hu, S. C. Tu, Dr. N. Tian, Prof. H. W. Huang, Prof. Y. H. Zhang
Beijing Key Laboratory of Materials Utilization of Nonmetallic Minerals and Solid Wastes, School of Materials Science and Technology
China University of Geosciences, Beijing 100083, P. R. China
E-mail: hhw@cugb.edu.cn; tianna65@cugb.edu.cn
- [b] Dr. T. Y. Ma
Discipline of Chemistry
University of Newcastle
Callaghan, NSW, 2308, Australia
E-mail: Tianyi.Ma@newcastle.edu.au

Abstract: Efficient conversion of solar energy by means of photocatalysis shows huge potential to relieve energy crisis and environmental pollution. However, the unsatisfied conversion efficiency still hinders its practical application. Introduction of external fields can remarkably enhance the photocatalytic performance of semiconductors from the inside out. This review focuses on the recent advances in the diversified external fields, involving the microwave, mechanical stress, temperature gradient, electric field, magnetic field and coupled fields, boosted photocatalytic reactions, including contaminant degradation, water splitting, CO₂ reduction and bacterial inactivation. The relevant reinforcement mechanisms of photoabsorption, transport and separation of photoinduced charges and adsorption of reactions by the external fields are highlighted. Finally, the challenges and future outlook for the development of external field enhanced photocatalysis are presented.

1. Introduction

Effective utilization of the primitive and abundant energies on the earth, such as solar, thermal and mechanical energy, shows tremendous potential to produce the storable chemical fuels and remove environmental contaminants. Among them, photocatalysis has been extensively investigated for H₂ evolution, CO₂ reduction, N₂ fixation and environmental purification.^[1] There are three crucial steps involved in a typical photocatalytic process: i) the generation of charge carriers; ii) the separation and transfer of charge carriers; and iii) redox reactions on the surface of photocatalysts.^[2] Aiming to improve the efficiency of each step, different strategies have been applied. For instance, energy band engineering, including element doping and heterostructure construction, have been conducted to enhance the visible-light absorption of photocatalysts, which is conducive to generation of more photoexcited charges.^[3] The established internal electric fields at the heterojunction interface and the depolarization fields existed in the single-domain ferroelectric materials have been proven to be efficacious in suppressing the recombination of electron-hole pairs.^[4] Defects and surface sites engineering of semiconductors can facilitate the adsorption and activation of reactant molecules.^[5] However, the modification of photocatalysts is always accompanied by the variation of geometries, compositions and components as well as the complex preparation process, which largely limit its wide application.

Introduction of external fields into the photocatalytic reaction system is a flexible and controllable strategy to enhance the photocatalytic activity without changing the pristine properties of semiconductors. For example, photoelectrocatalysis achieved an improved solar energy conversion efficiency by promoting the separation of photogenerated carriers with the applied external

bias.^[6] However, the photoelectrodes with high performances are usually prepared by in-situ growth method to get close contact between the photocatalysts and transparent conductive substrates, which cannot be effectively achieved for most of particulate photocatalysts.^[7] The development of the substitutable external fields and utilization of electric field in a new form are of great significance for efficient surface reactions of powdery catalysts. To date, it has been reported that many external fields, including the microwave, piezoelectric, pyroelectric, electric poling, magnetic fields and the coupling of them, have the capability to improve the charge separation and consequently the photocatalytic performance of semiconductors.^[8] Taking the microwave irradiation as an example, the resulting defect sites at the surface of semiconductors serve as the electron traps to suppress the carrier recombination.^[9] While more efficient charge separation can be realized by exerting the external strain, temperature fluctuation and electric poling, which will generate the positively and negatively polarized charges on the two sides of the polar catalysts, establishing an electric field across the catalyst that drives the separation of photogenerated electron-hole pairs in both bulk phase and on the surface.^[10] Besides, the magnetic field induced Lorentz force and electron polarization can also provide a strong driving force to separate the photoexcited electrons and holes to opposite directions.^[11] Nevertheless, the effects of the external fields on the band structures and surface properties of photocatalysts are always neglected, such as the improved optical absorption by microwave non-thermal effects, electrically tunable band gaps, and the ferroelectric polarization-induced molecule adsorption.^[12] Therefore, the clear, deep and systematic understandings on the functions of external fields in promoting the photocatalytic performance of semiconductors is of great significance and highly anticipated.

Recently, several excellent reviews focusing on the photocatalytic performance of the piezoelectric, pyroelectric and ferroelectric semiconductors have been published. Pan et al. summarized the piezo-phototronic effect enhanced photocatalytic and photoelectrocatalytic processes, in which the tunable band bending and charge migration were stressed.^[13] Our group reviewed the polarization improved bulk and surface charge separation and highlighted the roles of different polarization fields in photocatalysis.^[10] Wang et al. focused on the piezo-/pyro-/ferro-potential induced built-in electric field and summarized the corresponding catalytic applications.^[14] Li et al. introduced the recent advances of ferro-, piezo-, and pyroelectric nanomaterials for various catalytic applications, and the influences of internal electric field in carrier separation and transport were discussed.^[15] However, almost all the above-mentioned reviews concentrated on the internal electric field in polar photocatalysts, whereas the functions of external fields in photocatalysis were paid few attentions.

REVIEW

WILEY-VCH

In this review, we summarize the recent advances of various types of external fields, including microwave, mechanical stress, temperature gradient, external electric field, magnetic field and the coupled fields, promoted photocatalytic performance in water splitting, CO₂ reduction, bacterial inactivation and pollutant degradation. Moreover, the origins of significant enhancement of photocatalytic activity by external fields are highlighted, including the improved photoabsorption, charge separation, adsorption and activation of reactants (**Figure 1**). Finally, the challenges and future outlook for the development of external fields assisted photocatalysis are presented.

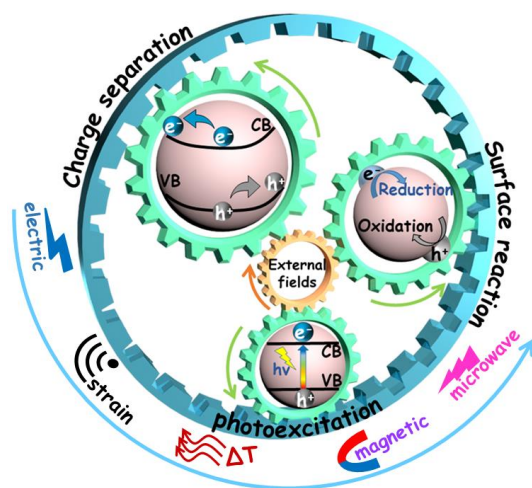


Figure 1. Schematic diagram of the external fields improved photocatalytic processes.

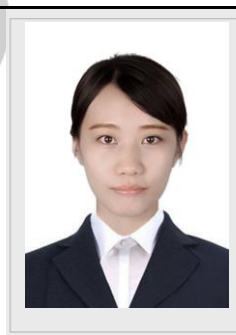
2. Microwave field

Microwave radiation, which is the electromagnetic wave with a frequency of 300 MHz-300 GHz, has been extensively applied in the area of organic synthesis to replace the traditional heating technology.^[16] Due to the fast and uniform microwave heating accelerating chemical reactions, the introduction of microwave field into the photocatalytic processes, particularly the advanced oxidation processes, has attracted considerable interests.^[17] In general, microwave irradiation enhances the photocatalytic performance of semiconductors in two ways, namely thermal and non-thermal (specific) effects. The photocatalytic activity improvement derived from microwave thermal effect is similar to that by the thermal catalytic process, which can be described as that the increase of reaction temperature speeds up the surface redox reactions. Meanwhile, owing to the thermal excitation and lattice thermal vibration of catalysts, the carrier concentration is increased.^[18] However, many studies have proposed that the remarkable enhancements on photocatalytic reaction dynamics not only stem from the thermal effect, but also are largely contributed by the non-thermal effect related to the surface properties of catalysts.^[19]

To investigate the microwave specific effect, the photoreactor was placed in a microwave generator equipped with a light source and cooling system to maintain the ambient temperature (**Figure 2a**).^[20] It was elaborated that the influence of the non-thermal effect on the photocatalytic processes is mainly reflected by the variation of optoelectronic and surface properties of semiconductors under the microwave field. For instance,

Horikoshi et al. in situ observed the typical double-band-like absorption spectrum of P-25 TiO₂, of which the band edge was located at 400 nm (3.09 eV) and 365 nm (3.39 eV), respectively. After 10 min of microwave irradiation, the light absorption of TiO₂ was obviously extended to the visible region (**Figure 2b**). The formation of this characteristic absorption peak is attributed to the emergence of additional defect sites such as oxygen vacancies and cation vacancies on the surface of catalysts. Thus, a defect level was introduced into the band gap to broaden the optical response range of semiconductors by increasing the transition probability of valence band (VB) electron or narrowing the band gap with the hybridization of the donor level and conduction band (CB).^[21]

Na Tian is a Lecturer at the Beijing Key Laboratory of Materials Utilization of Nonmetallic Minerals and Solid Wastes, School of Materials Science and Technology, China University of Geosciences (Beijing). She received her Ph.D. in 2018 from the School of Materials Science and Technology, China University of Geosciences (Beijing). Her research focuses on the design and synthesis of photocatalysts for environmental purification, photocatalytic H₂ generation and CO₂ reduction.



Tianyi Ma received his Ph.D. in Physical Chemistry in 2013 from Nankai University, China. He then worked as a postdoctoral research fellow from 2013 to 2014 at University of Adelaide, Australia. He was awarded the Australian Research Council (ARC) Discovery Early Career Researcher Award (DECRA) in 2015. He is currently a Senior Lecturer in Discipline of Chemistry at University of Newcastle, leading an independent research group focusing on energy materials and catalysis.



Hongwei Huang is a Professor in School of Materials Science and Technology at China University of Geosciences (Beijing). He received his Ph.D. in 2012 from Technical Institute of Physics and Chemistry, Chinese Academy of Sciences, and worked as a visiting scholar in the lab of Prof. Thomas Mallouk in The Pennsylvania State University (2016-2017). His current research mainly focuses on the crystal structural design and charge regulation of layered photocatalytic nanomaterials and their applications for environment and energy.



Besides, the surface defect sites can also serve as the electron traps to suppress the charge recombination and prolong the lifetime of photoexcited carriers (**Figure 2f**). In a typical case, picosecond transient absorption spectroscopy was utilized to in situ investigate the charge carrier dynamics of wetted TiO₂ under microwave irradiation. A slower decay of transient absorption at the probe wavelength in the TiO₂/H₂O system indicated that the

REVIEW

WILEY-VCH

recombination of photogenerated electrons and holes followed slow decay kinetics under microwave irradiation owing to the additional defects induced by the non-thermal effect (Figure 2c).^[22] Furthermore, it was reported that the surface properties of TiO₂ can be effectively mediated by microwave irradiation, including the surface reactant adsorption and hydroxyl activation. Hidaka and co-workers developed an in situ electron spin-resonance (ESR) technology to examine the production of hydroxyl radicals formed in the rutile TiO₂ under simultaneous ultraviolet light (UV) and microwave (MW) irradiation. The ESR signals of the DMPO-hydroxyl radicals ($\cdot\text{OH}$) spin adducts were stronger under both UV and MW irradiation than that under UV irradiation at 18 or 22 °C, illustrating that the microwave non-thermal effect might activate the surface hydroxyls to generate more free hydroxyl radicals in the TiO₂/H₂O system (Figure 2e).^[23] This result was further confirmed by the transformation of the hydrophilicity on TiO₂ surfaces, where the intrinsic hydrophilic TiO₂ surfaces became hydrophobic after irradiation with MW and UV, due to the changes of the amount of surface hydroxyls (Figure 2h).^[24] Moreover, the hydrophobic surfaces of photocatalysts will facilitate the adsorption of alkyl groups, promoting the efficiency of advanced oxidation processes for organic contaminants (Figure 2g). Bian et al. probed the role of the microwave field in reactant adsorption on the surface of TiO₂ by Raman spectroscopy. The remarkably increased Raman peak intensity at 750 and 1587 cm⁻¹ under both MW and UV irradiation illustrated the improved molecular adsorption, resulting in an efficient degradation performance for p-chlorophenol (4-CP) and methyl orange (MO) (Figure 2d).^[25]

Hence, the enhanced optical absorption, charge separation, reactant adsorption and hydroxyl activation can reasonably interpret the high efficiency of microwave-assisted photocatalytic oxidation processes, which have been satisfactorily applied to degrade industrial pollutants, such as methylene blue (MB), 2,4-dichlorophenoxyacetic acid, 4-chloro 2-aminophenol, 1, 1, 1-trichloro-2, 2-bis (p-chlorophenyl) ethane, atrazine, and nitrobenzene.^[26] Nevertheless, the microwave field improved surface activity of semiconductors is limited, in which the recombination of electrons trapped in the deep traps still restrains the photocatalytic activity. Developing other external fields to provide driving force for efficient photocatalytic process is still essential.

Figure 2. (a) Schematic illustration of the microwave-/photo reaction device with a cooling system. Adapted with permission from Ref [20]. Copyright 2009 Elsevier. (b) Absorption spectrum of P-25 TiO₂ after 10 min of MW irradiation calculated from the diffuse reflectance spectra. Adapted with permission from Ref [21]. Copyright 2009 American Chemical Society. (c) Decay of transient absorption with and without microwave irradiation for TiO₂/H₂O system. Adapted with permission from Ref [22]. Copyright 2015 Royal Society of Chemistry. (d) Raman spectra of Ag/TiO₂ under different reaction conditions for 15 min reaction. Adapted with permission from Ref [25]. Copyright 2019 Elsevier. (e) In situ ESR spectral of the DMPO- $\cdot\text{OH}$ spin adducts under different reaction conditions. Adapted with permission from Ref [23]. Copyright 2003 Elsevier. (f) Schematic illustration of the enhanced surface charge separation by microwave non-thermal effect. (g) Schematic illustration of the microwave-assisted photocatalytic oxidation processes. (h) Schematic illustration of the changes in surface properties of semiconductors under microwave irradiation.

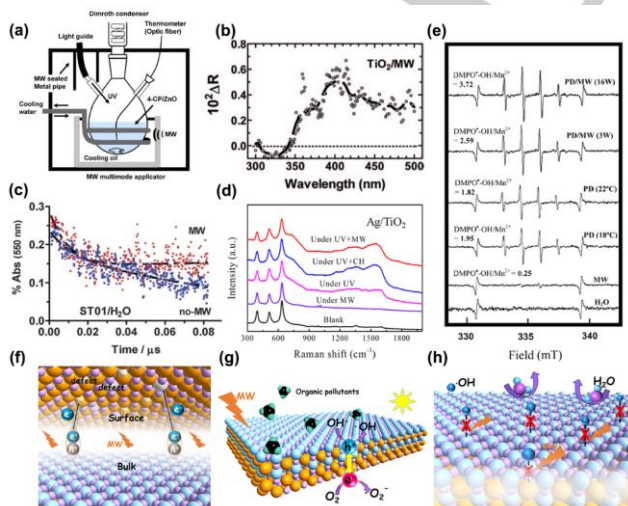
3. Mechanical stress field

External mechanical stress harvested by piezoelectrics can induce the generation of piezopotential that can be utilized to directly trigger catalytic reactions, which is known as piezocatalysis. For piezoelectric semiconductor or the composites consisting of piezoelectric insulator and semiconductor, the coupling of light and mechanical stress achieves the piezocatalytic and photocatalytic reactions, and may greatly enhance the photocatalytic process. Under the applied strain, piezoelectrics originated from the non-centrosymmetric crystalline structure can generate the piezoelectric potential and polarized charges. It can not only facilitate the separation of charge carriers in bulk and on the surface of the semiconductors, but also effectively modulate the barrier height to tune the carrier migration at the interface of heterojunction, known as the piezophototronic effect.^[27] As the piezoelectric potential and band bending can promote the migration of electrons and holes to opposite surfaces, the redistribution of redox active sites on the surface of photocatalysts can be also achieved. The spatially separated redox reactions prevented the reverse reaction between reduction and oxidation products.^[28] Hence, introduction of the mechanical stress field provided by the high-frequency ultrasonic vibration, low-frequency shear force and mechanical brushing/sliding is an efficient tactic to improve the photocatalytic activity of piezo-semiconductors.

3.1. High-frequency ultrasonic vibration

Ultrasonic irradiation is the most common approach to generate the periodic external strain on piezoelectrics and deform them effectively due to the extreme acoustic pressure of ultrasonic waves and the local high pressure induced by the collapse of active bubbles.^[29] The strength of the mechanical stress field can be easily adjusted by controlling the ultrasonic power and frequency to optimize the reaction parameters.

The ultrasonic-assisted photocatalytic reaction system can be easily realized by equipping the photoreactor into an ultrasonic cleaner (Figure 3a). In this coupled system, the ultrasonic vibration can induce the deformation of piezoelectric semiconductors, which leads to the deviation of positive and negative charge centers in the unit cell. Thus, a polarization-induced internal electric field is generated to promote the migration of electrons and holes along opposite directions, and remarkably enhance the photocatalytic performance (Figure 3b).^[13] Therefore, the piezoelectrics with the one/two-dimensional (1D/2D) structures that are more easily deformed can trigger much greater piezopotential inside the materials. For



instance, the distribution of piezoelectric potential in BaTiO₃ with different morphologies under ultrasonic irradiation was simulated by the finite element method (FEM). The BaTiO₃ nanowire undergoing a 10⁸ Pa pressure was predicted to produce the maximum potential difference up to 11.16 V, which is much greater than that of the BaTiO₃ nanoparticle (**Figure 3c**).^[30] Similarly, the KNbO₃ nanosheet also showed a much higher potential output than the nanocube counterpart under ultrasonic excitation.^[30b]

Zhao et al. reported that the CdS ultrathin nanosheets exhibited a significantly enhanced H₂ evolution performance under light and ultrasonic irradiation, which is more than twice as high as the sum of light and vibration individually (**Figure 3d**).^[31] It indicated that the photocatalytic activity of CdS was remarkably improved with the assistance of ultrasonic vibration. Both the improved carrier separation and enriched surface active sites contributed to the efficient H₂ production of CdS nanosheets. Some niobates are typical ferroelectric perovskites, such as LiNbO₃, NaNbO₃, etc. which showed benign photocatalytic performance. Hence, they are suitable candidates to investigate the mechanical stress field enhanced photocatalytic applications. Singh et al. prepared the piezoelectric NaNbO₃ nanorods and achieved an enhanced MB degradation rate by coupling of the photoexcitation and ultrasonic vibration, which led to an effective separation of photoinduced electrons and holes in the bulk phase (**Figure 3e**).^[32] The ultrasonic-assisted piezophototronic effect enhanced the photocatalytic formation of superoxide radicals ($\bullet\text{O}_2^-$) and $\bullet\text{OH}$, which oxidized the MB molecules to CO₂ and H₂O. In another study, oxygen vacancies were introduced to extend the photoresponse of ZnSnO₃ to the visible region, which enhanced the ultrasonic-assisted photocatalytic activity. Under simultaneous ultrasonic and visible light irradiation, the ZnSnO₃ with oxygen vacancies demonstrated a superior H₂ evolution performance with a rate of 6000 $\mu\text{mol}\cdot\text{g}^{-1}$, providing an effective tactic to modulate the piezo-photocatalytic activity.^[33] In addition to the efficient charge separation in bulk, the distributions of surface active sites can also be effectively manipulated by ultrasonic-induced piezoelectric polarization. Our group reported that the Sillén-Aurivillius structured Bi₄NbO₈X (X = Cl, Br) polar single-crystal nanosheets can generate reactive oxygen species (ROS) efficiently through the ultrasonic-assisted photocatalytic process.^[34] The piezoelectric potential rendered the formation of internal electric field and band bending, which not only facilitated the separation of photogenerated charges in the bulk, but also enriched the reductive reactive sites on {110} side facets and {001} top facets of Bi₄NbO₈X, benefiting for the oxygen reduction reaction (**Figure 3f**). As a result, the largely increased $\bullet\text{O}_2^-$, $\bullet\text{OH}$, and H₂O₂ production was obtained over Bi₄NbO₈X nanosheets under simultaneous visible light and ultrasonic irradiation.

Compared with the single-component piezoelectric semiconductor, the hybrid catalysts consisting of piezoelectrics and semiconductors may show a significantly enhanced piezoelectric potential output under ultrasonic irradiation. For instance, the theoretically calculated surface potential difference of BiOBr/BaTiO₃ reached 100 mV with a cavitation pressure of 10⁸ Pa, which far exceeded that of BaTiO₃ (31.21 mV) and BiOBr (30 mV), respectively. The large piezoelectric potential drives the charge carriers to separate efficiently, resulting in a high catalytic activity under light irradiation with auxiliary ultrasonic vibration.^[35] Through the combination of two typical piezoelectrics, the maximal piezoelectric potential difference of

414.40 mV was achieved for ZnO/BaTiO₃, which is much higher than those of BaTiO₃ and ZnO individually under the same external pressure. The enhanced macroscopic polarization led to an efficient charge separation and a sufficient mechanochemical potential to promote the catalytic reactions. As a result, ZnO/BaTiO₃ exhibited a prominent rhodamine B (RhB) degradation performance under both ultrasonic and light irradiation, with the degradation efficiency reaching 97% within 30 min.^[35b]

In heterojunctions, the space charge region and energy barrier at the interface can be effectively modulated by the ultrasound induced surface band bending, which further improves the photocatalytic performance by synergism of the interfacial potential difference and piezoelectric potential difference. For instance, the piezo-enhanced plasmonic photodegradation of MO was realized on Au/BaTiO₃ Schottky junction. The strengthened local electric fields surrounding the Au nanoparticles (NPs) allowed efficient separation and transport of photoexcited hot electrons from Au NPs to the adjacent BaTiO₃ owing to the surface plasmon resonance (SPR) effect. Ultrasonic stimulation produced the polarized charges from BaTiO₃ owing to the piezoelectric effect, which induced a downward band bending at the contact interface between BaTiO₃ and Au. It further reduced the energy barrier height and promoted the hot electron migration, leaving more excited holes on the Au NPs surface to directly or indirectly participate in the oxidation reactions (**Figure 3g**).^[36] Besides, the piezo-phototronic effect also takes a part in type-II heterojunctions. In a typical case, efficient catalytic degradation of MB was achieved for type-II CuS/ZnO nanowires under both solar light and ultrasonic irradiation. The spontaneous local electric field formed in the boundary contact region of CuS/ZnO facilitated the photoinduced electrons from the CB of CuS to transfer to that of ZnO, while the photogenerated holes migrated in the opposite direction. With the assistance of piezoelectric potentials generated by ZnO nanowires under ultrasound stimulation, electrons and holes were further separated and reached the surfaces of CuS/ZnO heterojunctions to participate in the redox reactions rapidly (**Figure 3h**).^[37] Wang et al. synthesized TiO₂/ZnO type-II heterojunction for piezo-photocatalytic H₂ production and discussed the relevant mechanisms. The ultrasonic irradiation induced band bending at the ZnO interface, which promoted not only the separation of photoexcited carriers in ZnO and TiO₂, but also the migration of electrons and holes at the interface with a space charge region. This fields coupling effect resulted in a higher H₂ production rate of TiO₂/ZnO under solar and ultrasonic irradiation, ~1.6 times of that in the photocatalytic process only.^[37b]

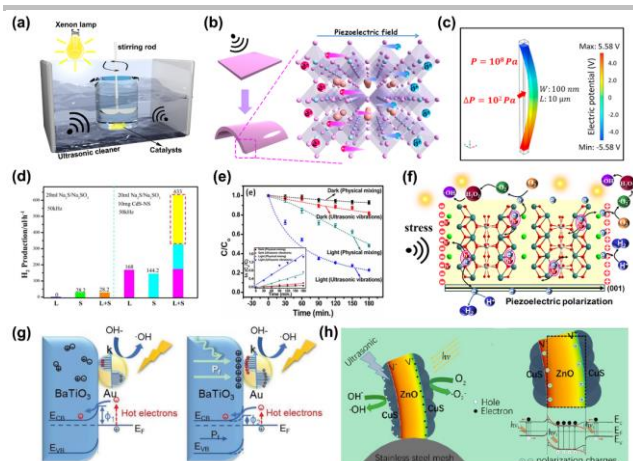


Figure 3. Schematic illustration of (a) the ultrasonic-/photo reaction device and (b) the mechanism of the ultrasound assisted photocatalytic reactions. (c) Theoretical simulation of the distribution of piezopotential in BaTiO₃ nanowire with 10⁸ Pa pressure applied. Adapted with permission from Ref [30]. Copyright 2018 Elsevier. (d) The rate of water-splitting hydrogen evolution over CdS under visible light irradiation (L), ultrasonic vibration (S), and light and ultrasonic irradiation (L+S), respectively. Adapted with permission from Ref [31]. Copyright 2019 Royal Society of Chemistry. (e) The photocatalytic degradation efficiency of NaNO₃ under different experimental conditions. Adapted with permission from Ref [32]. Copyright 2017 Elsevier. (f) Schematic illustrating the mechanism of ROS evolution through the piezo-photocatalytic process over Bi₄NbO₈X (X = Cl, Br). Adapted with permission from Ref [34]. Copyright 2019 Wiley. (g) Schematic illustration of the piezotronic effect improved plasmonic photocatalytic process. Adapted with permission from Ref [36]. Copyright 2019 Wiley. (h) Schematic illustration of the piezo-photocatalytic mechanism of the CuS/ZnO II-type heterojunction. Adapted with permission from Ref [37]. Copyright 2016 American Chemical Society.

3.2. Low-frequency shear force

Ultrasound is hard to be applied in large-scale industrial applications due to its intense energy input, which extremely limits the realistic application of the ultrasound-assisted photocatalysis. Developing other forms of mechanical stress, such as mechanical-stirring-induced shear force, to enhance the photocatalytic performance is of important practical significance. Different from ultrasonic vibration, the fluid-generated pressure is much weaker to trigger the large potential in piezoelectric semiconductors. Utilization of the piezoelectric materials with highly mechanical sensitivity to harvest the low-frequency flow disturbances effectively is an available approach for these stirring-assisted photocatalytic reactions.^[38]

As an ideal material to convert the mechanical energy, piezoelectric polymer film with the favorable light transmissivity can capture the tiny momentum sensitively. For example, CdS was loaded on the porous composite polymer film of 4-azidotetrafluorobenzoic acid-treated graphene hybridizing with poly(vinylidene fluoride-co-hexafluoropropylene) (rGO-F/PVDF-HFP) to demonstrate the piezo-photocatalytic H₂ production under the magnetic stirring and illumination simultaneously (Figure 4c).^[39] The mechanical disturbances of water flow generated the long-lasting piezoelectric potential that enhanced the separation of photogenerated electrons and holes. Also it provided free electrons from the rGO-F fillers even without light irradiation. Both above-mentioned advantages contributed to the improved H₂ productivity of the hybrid with a rate of 10.4 μmol·h⁻¹·g⁻¹. Besides, by integration of the piezoelectric PVDF film with (100) polar plane exposed ZnO, the piezoelectric potential was further enhanced due to the dual-piezoelectric

response of the hybrid under magnetic stirring, which promoted more electrons and holes to separate and migrate to the surface for photodegradation reactions.^[39b] In addition to stirring, bubble flow was employed to generate piezopotential in PVDF-TiO₂ hybrid. With the air bubbling and UV irradiation, the degradation efficiency of MB was enhanced by 99% compared with the photocatalytic counterpart.^[39c]

One of the other strategies for harvesting the low-frequency shear force of water flow is utilizing the ferroelectric materials with large piezoelectric coefficients in the stirring-driven piezo-photocatalytic system. Bian et al. achieved direct degradation of organic dyes by lead zirconate titanate (PZT) microspheres at a stirring rate of 300 rpm, illustrating that PZT collected the discrete energy from water and created a piezoelectric potential to separate the free charges, even without 1D or 2D structures that were easily deformed.^[38] Moreover, the PZT/TiO₂ core-shell hybrid showed significantly improved RhB degradation activity with total decolorization within 80 min under 800 rpm of magnetic stirring and light irradiation (Figure 4d). The fluid-induced piezoelectric potential and polarized charges in PZT core promoted the separation of photogenerated electron-hole pairs from TiO₂ shell, leading to the boosted degradation performance (Figure 4e).^[40]

Although the flow-generated piezoelectric potential is relatively weak, coupling with the internal electric field derived from the heterojunction can effectively enhance the piezo-phototronic effect induced by discrete fluid mechanical energy. For instance, the Z-scheme ZnO/WO₃ (Zn-W-5) hybrid showed a photocurrent density of 3.38 mA cm⁻² at 1.23 V vs. RHE with a stirring rate of 1000 rpm, which is 3.02 times higher than that of pure ZnO.^[41] Only the vertical solution flow toward the photoanode surface bent the ZnO nanorods and generated the piezo-photocurrent efficiently (Figure 4f). In this process, the formation of direct Z-scheme junction improved the charge transfer and separation at the interface owing to the Fermi levels alignment between ZnO and WO₃, leading to the bending of band edges of the two semiconductors in the opposite directions. Ulteriorly, stirring induced piezoelectric polarized charges from ZnO, which tuned the Fermi levels and interface band bending to accelerate the charge transfer between ZnO and WO₃, significantly enhancing the photo-reactivity of this Z-scheme junction (Figure 4g).

3.3. Mechanical brushing/sliding

Though the aforementioned two forms of mechanical stress are easily implemented without a complicated reaction device, the stress intensity exerted on the surface of the piezoelectric semiconductors cannot be controlled precisely. To establish an accurate model for the mechanical stress field assisted photocatalytic process, some special devices, such as the cantilever connected with the piezoelectric material, were designed.^[14] It should be noted that the piezoelectric semiconductors must be sampled into a flexible device to undergo the brushing, sliding, shaking or compression. For instance, Xue et al. designed a piezo-photocatalytic system composed of the ZnO nanowires arranged vertically on carbon fibers (CFs).^[42] Several bunches of ZnO nanowires/CFs were woven together to form multi-fibers structure, which enabled the nanowires to extrude outward radially and against each other by the externally applied force (Figure 4a). With the applied UV light irradiation and periodic force, the photoinduced electron-hole pairs from ZnO were rapidly separated and migrated to the

REVIEW

WILEY-VCH

opposite surfaces owing to the piezoelectric potential generated by the bending of ZnO nanowires (**Figure 4b**). Furthermore, the piezoelectric potential in ZnO/CFs could be constantly enhanced by increasing the frequencies of the applied force, resulting in a high piezo-photocatalytic degradation efficiency of MB solution, which reached 98.8% in 120 min. In addition to the multi-fibers device, ferroelectric $\text{Pb}(\text{Mg}_{1/3}\text{Nb}_{2/3})\text{O}_3\text{-}32\text{PbTiO}_3$ (PMN-PT) film was attached to a cantilever for H_2 evolution under the periodic mechanical oscillation, in which the bended ferroelectric film generated a sufficient piezoelectric potential to drive the H^+ reduction reactions.^[42b] However, these piezoelectric devices that harvest the physical forces are still rarely used for photocatalytic applications, partially because the source of mechanical energy is limited to the artificial stress. The coupling of solar energy and the other forms of mechanical energy needs to be exploited for energy and environmental applications.

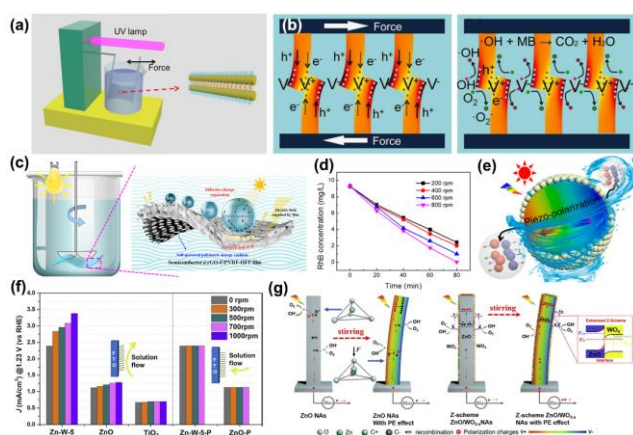


Figure 4. (a) The degradation of MB solution by the piezo-photocatalytic process over ZnO nanowires/CFs. (b) Schematic illustration of the working mechanism for the piezo-photocatalytic degradation process. Adapted with permission from Ref [42]. Copyright 2015 Elsevier. (c) Schematic illustration of the stirring-/photo reaction device and the hydrogen production process of the rGO-F/PVDF-HFP-CdS polymer film. Adapted with permission from Ref [39]. Copyright 2018 Elsevier. (d) Photocatalytic degradation of RhB over PZT/TiO₂ under different stirring rates. (e) Diagram illustration of the fluid-induced piezo-photocatalytic process. Adapted with permission from Ref [40]. Copyright 2018 American Chemical Society. (f) The photocurrents of Zn-W-5, ZnO and TiO₂ under different stirring rates and water flow directions. (g) Schematic illustration of the piezoelectric polarization enhanced Z-scheme effect in ZnO/WO₃. Adapted with permission from Ref [41]. Copyright 2019 Elsevier.

4. Temperature gradient field

The temperature oscillation can be scavenged and converted into electrical and chemical energies based on the pyroelectric effect that originates from the polarization in pyroelectric materials. It provides a promising route to enhance the solar energy conversion efficiency by integration of pyroelectricity and semiconductor characteristics, namely, the pyro-phototronic effect.^[43] Different from the piezoelectrics discussed above, pyroelectric materials can generate dipoles spontaneously in crystals even without strain, whereas the polarized charges may be completely screened by free carriers and the charges in surrounding electrolyte. When the temperature fluctuation breaks the thermodynamic equilibrium, the variation of polarization will induce the generation of pyro-potentials along the crystal. The as-appeared positive and negative polarized charges at both ends can be utilized to enhance the charge

separation efficiency and to effectively modulate the photoinduced carriers transport across the junction interface (**Figure 5**).^[44] In this process, the generated pyro-potential can also alter the surface charge energy to directly trigger catalytic reactions, called pyrocatalysis, which cooperates with the photocatalytic process for efficient pyro-photocatalytic reactions. Nowadays, some typical pyroelectrics, such as ZnO and CdS, have been extensively applied in solar cells and photodetectors. However, the incorporation of pyro-phototronic effect resulted by temperature gradient to improve the photocatalytic performance is still in the embryonic stage.^[45]

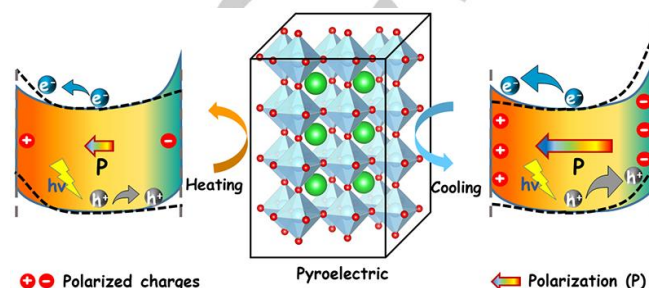


Figure 5. Schematic illustration of the pyro-phototronic effect modulated charge separation and transfer in pyroelectrics.

In general, there are two frequently used methods to generate the temperature gradient field in photocatalytic processes, one of which is to set up thermal cycles by heating and cooling the reaction system in a water bath with a certain interval (**Figure 6a**). For example, the enhanced catalytic RhB decomposition was achieved by ZnSnO₃ NPs under the excitation of UV light and 20-65 °C thermal cycles, where the degradation ratio reached up to 98.1% with 8 thermal cycles, much higher than the decomposition ratios by photocatalysis (76.8%) and pyrocatalysis (20.2%).^[46] The temperature alternation resulted in the formation of pyroelectric field, which facilitated the separation of photoexcited electron-hole pairs, thus accelerating the reactive radicals to participate in the degradation reactions. Some other materials, like Cu doped ZnS also showed improved photocatalytic degradation performance under temperature gradient field.^[46b] Besides, Liu et al. utilized the rapid temperature oscillation method to produce pyroelectric potentials to deposit Au NPs on the surface of BaTiO₃, providing an alternative strategy to fabricate the metal-pyroelectric hybrid materials for efficient photocatalytic reactions.^[46c]

Photothermal effect can realize the efficient light-to-heat conversion, which provides another approach to localize the light and heat energy simultaneously by exerting the periodical solar irradiation on the pyro-semiconductors and photothermal materials. For instance, a heat-collecting catalytic reaction system was fabricated by a porous pyroelectric membrane floating at the liquid interface and a light source equipped with an optical chopper, which periodically blocked the incident solar light to achieve the heating and cooling processes (**Figure 6b**).^[47] Under light irradiation, the surface temperature was quickly increased by the carbon black film on the top of the pyroelectric membrane in several seconds, while the cooling process also took place fast when the incident light was blocked due to the high thermal heat capacity of water. Compared with the traditional thermal cycles, the photothermal conversion can utilize the infrared light and realize a relatively high rate of

REVIEW

WILEY-VCH

temperature change, which is beneficial to the pyro-photocatalytic process. On the basis of this effect, Dai et al. fabricated a new semi-immersion type heat collecting photocatalytic device, which was composed of the PVDF-HFP as pyroelectric substrate, carbon nanotube (CNT) as photothermal material and CdS photocatalyst (PVDF-HFP/CNT/CdS).^[47b] Upon infrared light irradiation, the heated CNT transferred the thermal energy to the PVDF-HFP microfiber, resulting in the establishing of pyroelectric field as a driving force to separate the photoexcited electron-hole pairs of CdS. After deposition of Pt on the surface of CdS, the segregated electrons further moved to Pt and generated H₂ efficiently, leading to a high photocatalytic H₂ generation rate of 451 $\mu\text{mol}\cdot\text{g}^{-1}\cdot\text{h}^{-1}$ with an average apparent quantum yield of 16.9% (**Figure 6c** and **d**).

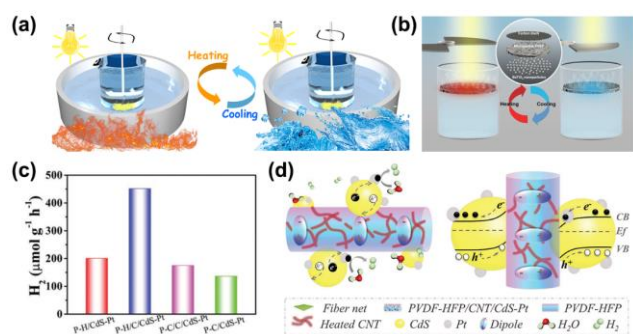


Figure 6. (a) Schematic illustration of the photocatalytic reaction system with heating and cooling cycles. (b) Schematic illustration of catalytic reaction system assisted by the photothermal effect. Adapted with permission from Ref [47]. Copyright 2018 American Chemical Society. (c) Photocatalytic hydrogen production rates of the obtained samples under Xenon lamp illumination without filter. (d) The transfer of photogenerated carriers and energy band bending at the interface of PVDF-HFP and CdS under light and temperature variation. Adapted with permission from Ref [47b]. Copyright 2020 Wiley.

5. External electric field

External bias has been extensively used to enhance the photocatalytic performance by accelerating the separation of photoinduced carriers, which develops into the photoelectrocatalysis (PEC) for efficient solar energy conversion. Nevertheless, charge recombination occurring in the bulk of the semiconductor photoelectrodes still significantly reduces the photoconversion efficiency; the long migration distance and weak driving force of charge carriers also hinder the efficient surface reactions in electrolyte.^[7] Utilization of the external bias induced polarization effect to enhance the photocatalytic activity provides a new approach to the design of electric field assisted photocatalytic system. In this section, we will discuss the functions of the electric field on the photocatalytic performance by two means: the in situ external electric field induced constant electric field effect, and electric poling pretreatment augmented ferroelectric polarization.

5.1. In situ external electric field

We describe the effects of an external electric field on the electronic structures and electric dipoles of semiconductors as the electric field effect, which modulates the generation, separation and transport of photogenerated charge carriers. Recently, it has been reported that the external bias was introduced into the photocatalytic reaction system by the bipolar

electrochemical (BPE) cell in a wireless way, making it available to take advantage of the electric field effect for efficient photocatalytic reactions of particulate photocatalysts. In a typical case, anisotropic Au-TiO₂ Janus particles were synthesized by the synergy of BPE and photochemistry, and the electric field assisted photoreduction mechanism was revealed.^[48] The BPE reaction cell was equipped with a UV light source, in which TiO₂ particles and the metal salt were placed in a channel connected with two electrode compartments to provide the electric field (**Figure 7a**). After applying the electric field and UV light irradiation for 60 s, almost all Au particles were located at the δ^+ side, indicating that the photoinduced electrons were selectively separated and transferred to the surface of TiO₂ for reduction reactions (**Figure 7b**). The external electric field induced polarization effect and band bending, facilitating the transfer of charge carriers to the opposite sides of the particles, leading to the formation of the metal-TiO₂ Janus objects (**Figure 7c**). The generation of electric dipoles provided a strong driving force to separate the photogenerated electron-hole pairs, giving rise to efficient surface redox reactions for environmental remediation. Zhao et al. designed an electro-field assisted photocatalytic system based on the BPE cell for tributyltin (TBT) removal in tannery wastewater. The photocatalytic TBT degradation efficiency over TiO₂ microspheres with the applied external potential was almost a 9-fold enhancement compared to that without electro-field, of which the reaction rate constant of 0.0488 min^{-1} was achieved due to the suppressed charge recombination in bulk.^[48b]

Utilization of the electric field effect to modulate the electronic band structures of semiconductors can be explained by the well-known Stark effect, which leads to the splitting of energy band that narrows the band gap with a shift of VB and CB states.^[49] It has been reported that many 2D semiconductors possessed electrically tunable band gaps. Kim et al. realized a wide modulation of band gap in few-layer black phosphorus (BP) by potassium atom doping, which was ascribed to the giant Stark effect resulted by dopants-induced vertical electric field. From the density-functional-theory (DFT) calculations, the VB and CB levels will shift toward each other, resulting in the reduction of band gaps.^[50] Besides the materials with good conductive properties, the band gap modulation and even semiconductor-metal transition can also be achieved over typical TiO₂-based photocatalysts under the electric field.^[51] As shown in **Figure 7d**, all the orbital energy levels in the density of states (DOS) of TiO₂ gradually split and extended towards low energy region with the increase of electric field intensity. With applying electric field of 0.25 eV, the DOS of O 2p and Ti 3d orbitals crossed the Fermi level and the band gap of TiO₂ reduced to zero, accompanied by the transformation from semiconductor to metal. Consequently, the optical absorption of TiO₂ was significantly improved, and the absorption edges extended to the visible region when a 0.20 eV electric field was applied (**Figure 7e**). On account of the energy band shift, the redox abilities of photoinduced electrons and holes were also effectively modulated by the external potential. For instance, TiO₂ realized an enhanced decomposition efficiency of MB by 18% with the electric field assisted photocatalytic process.^[51b] The applied negative bias caused the upward movement of the CB edge, which led to a higher reduction potential for photoexcited electrons, promoting the oxygen reduction reaction to form $\cdot\text{O}_2^-$ participating in degradation processes. Although the theoretical basis of the electrically tunable band structures of

semiconductors is sufficient, it is still short of experimental evidence due to the lack of in situ detection technology.

The binding strength of reactants on the surface of catalysts largely depends on their electronic structures, which consequently can be effectively modulated by the external electric field. Ling et al. increased the H^+ adsorption on MoS_2 by optimizing the electronic structures of edges and defects of MoS_2 under different electric fields, and the tunable position of S p-resonance states was demonstrated to be dominant for binding strength and Gibbs adsorption free energy of H^+ .^[52] Yan et al. tuned the adsorption dynamics of VSe_2 nanosheets by applying a back gate voltage to greatly optimize the distribution of ions at the electrolyte- VSe_2 nanosheets interface for H_2 evolution reaction.^[52b] In addition to the improved hydrogen adsorption, some inert molecules like CO_2 also showed the electric field modulated adsorption characteristics. In a typical case, hexagonal boron nitride sheets (h-BN) became an effective adsorbent for CO_2 under an electric field.^[52c] The CO_2 molecule adsorbed on the h-BN sheet generated a nonzero dipole moment and slight bending, further contributing to the formation of stable adsorption configuration composed of positively charged C atoms in polarized CO_2 bonded with the negatively charged N atoms with the applied external potential (Figure 7f).

Hence, constructing the BPE cell assembled photocatalytic reaction system is an effective route to integrate the electric field effect, which substantially improved the photoabsorption, charge separation, and reactant adsorption of the particulate semiconductors without a complicated electrode molding process. It is also considered as a promising technology to increase the solar conversion efficiency with general applicability.

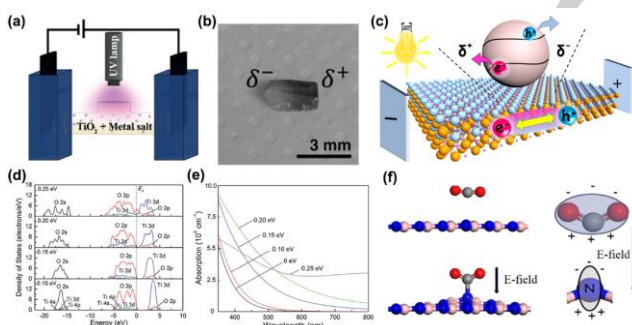


Figure 7. (a) Schematic diagrams of the bipolar electrochemical cell under simultaneous UV irradiation for deposition of Au on TiO_2 . (b) Optical microscopy of the macro- TiO_2/Au (the black region is the deposited Au). Adapted with permission from Ref [48]. Copyright 2017 Wiley. (c) Schematic illustration for the mechanism of the electric field effect enhanced charge separation. (d) The calculated DOS results of O atoms and Ti atoms of TiO_2 under different electric fields. (e) Absorption spectra of TiO_2 under different electric fields. Adapted with permission from Ref [51]. Copyright 2016 Royal Society of Chemistry. (f) The configuration of CO_2 molecule adsorbed on the h-BN sheet with the applied external electric field of 0.03 and 0.04 au. Adapted with permission from Ref [52c]. Copyright 2015 American Chemical Society.

5.2. Electric poling pretreatment

Ferroelectrics possess the spontaneous polarization with bound charges on the surface, which can be further enhanced by the external electric field. The as-formed strong ferroelectric field can largely facilitate the separation of bulk and surface charges in ferroelectric semiconductors. It is noteworthy that electric

poling is a pretreatment process for material modification before the photocatalytic reaction. Corona poling is a facile approach to directly exert the intense electric field on ferroelectric powder samples. In this process, the electric field is applied on the tip of a needle electrode to charge the material placing on the copper plate (Figure 8a). For instance, Park et al. prepared polarized $K_{0.5}Na_{0.5}NbO_3$ powder via a corona poling process and achieved a significantly enhanced photocatalytic H_2 production rate of $\sim 0.47 \text{ mmol}\cdot\text{g}^{-1}\cdot\text{h}^{-1}$, which is 7.4 times higher than that of the non-poled sample (Figure 8b).^[53] The strong ferroelectric field originated from the alignment of the ferroelectric domains under electric field provides an effective driving force to separate photogenerated electrons and holes in the bulk phase (Figure 8c). Our group reported the introduction of a strong ferroelectric polarization into thin-layered Bi_2MoO_6 by corona poling.^[53b] The coupling effect of ultrathin structure and ferroelectric polarization not only promoted the bulk charge separation, but also greatly enhanced the CO_2 adsorption of Bi_2MoO_6 . As a result, the polarized ultrathin Bi_2MoO_6 nanosheets exhibited an enhanced CO_2 photoreduction activity with CO production rate of $14.38 \text{ }\mu\text{mol}\cdot\text{g}^{-1}\cdot\text{h}^{-1}$, over 10 times increase than that of the non-poled bulk Bi_2MoO_6 (Figure 8d).

In addition to the corona poling, the external electric field can also be applied to the ferroelectric powders by fabrication of organic-inorganic composite films. In this process, ferroelectric particles were added into the organic solvent with the soluble organic polymer dissolved, and then the mixture was coated on a conductive substrate to conduct the electric poling (Figure 8e). Zhang et al. obtained the polarized Bi_2WO_6 nanosheets by first fabricating and electrically poling the polymethyl methacrylate (PMMA)/ Bi_2WO_6 composite film.^[54] The photocatalytic degradation rates for various contaminants over polarized Bi_2WO_6 increased by 2 times after electric poling, which originated from the prolonged carrier lifetime and the suppressed charge recombination under strong ferroelectric field. Similarly, Huang and coworkers used PMMA as the conductive substrate to pole ferroelectric $BiFeO_3$ powders, also realizing greatly improved photocatalytic activity.^[54b]

Poling pretreatment can also be conducted in an electrochemical cell with the ferroelectric electrode as the working electrode and Pt plate/FTO glass as the counter electrode (Figure 8f). It requires that the ferroelectric particles need to be in situ grown on conductive substrates to fabricate the photoelectrodes, so that the photocatalytic reactions can occur in a two-electrode system without any externally applied voltage. For instance, the positively poled $CdS/Au/Ti/Pb(Mg_{1/3}Nb_{2/3})_{0.7}Ti_{0.3}O_3$ ($CdS/Au/Ti/PMN-PT$) showed a considerably high solar-to-hydrogen conversion efficiency by the uniphotocatalytic cell system composed of the $CdS/Au/Ti/PMN-PT$ electrode and Pt electrode connected by an electric wire.^[55] The photoexcited electrons in the positively polarized $CdS/Au/Ti/PMN-PT$ directly transferred to the Pt electrode for efficient H_2 evolution due to the enhanced ferroelectric polarization promoting the charge separation and migration (Figure 8g). Consequently, the polarized sample achieved a stable H_2 production rate of $30 \text{ }\mu\text{mol}\cdot\text{cm}^{-2}\cdot\text{h}^{-1}$, which is much higher than the un-polarized sample under the same conditions (Figure 8h). The expected H_2 production rate calculated from the photocurrent exceeded the experimental one, indicating that the surface reaction kinetics were the dominant factors governing the photocatalytic performance instead of the charge separation process.

Because the polarization direction in ferroelectrics can be easily switched by the electrode poling process, the band bending at the interface of ferroelectric heterojunction can be effectively manipulated in a facile way, which provides a precise approach to modulate the interface band alignment. For instance, the construction of Z-scheme junction is difficult to achieve owing to the uncontrollable vectorial electron transfer between the photocatalytic reduction system (PS I) and oxidation system (PS II). However, ferroelectric materials with the tunable band bending can solve this problem effectively. Li et al. constructed the $\text{BiVO}_4\text{-BiFeO}_3\text{-CuInS}_2$ ternary Z-scheme junction by tuning the interfacial band bending of BiFeO_3 with different poling directions.^[56] Without any electric field, electrons are unable to transfer from the CB of BiVO_4 and BiFeO_3 to the VB of CuInS_2 , because of the high energy band barrier between them. After the anode was poled, the polarization-induced electric field in BiFeO_3 enabled the downward band bending at the $\text{BiFeO}_3/\text{CuInS}_2$ interface to realize a reduced energy barrier, which impelled the recombination of photogenerated electrons from BiFeO_3 and holes from CuInS_2 to form a Z-scheme junction with prominent photocatalytic activity. However, exerting reversed electric field allowed the holes to migrate from BiFeO_3 to CuInS_2 and then combined with the electrons in CuInS_2 , which decreased the PEC performance of $\text{BiVO}_4\text{-BiFeO}_3\text{-CuInS}_2$ ternary Z-scheme junction (Figure 8i).

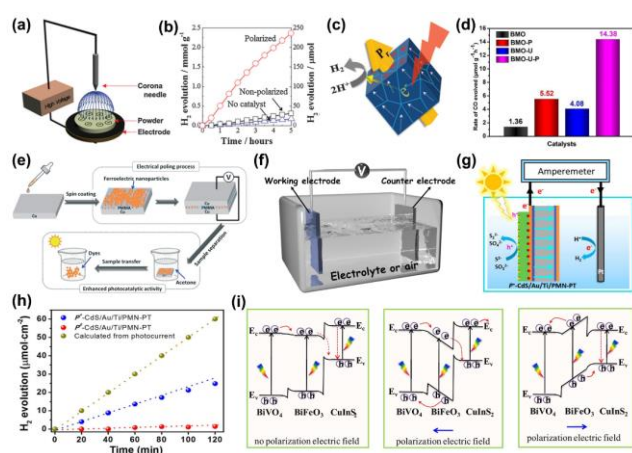


Figure 8. (a) Schematic diagram of the corona-poling system. (b) Photocatalytic hydrogen production rates of the polarized and non-polarized $\text{Na}_{0.5}\text{K}_{0.5}\text{NbO}_3$ powders. (c) The polarization behavior of a semiconductor after corona-poling. Adapted with permission from Ref [53]. Copyright 2014 Royal Society of Chemistry. (d) Photocatalytic CO production rate of the poled ultrathin Bi_2MoO_6 nanosheet. Adapted with permission from Ref [53b]. Copyright 2020 Royal Society of Chemistry. (e) Schematic illustration of the electrical poling process by using an organic inorganic composite film as a conductive substrate. Adapted with permission from Ref [54]. Copyright 2018 Royal Society of Chemistry. (f) Schematic diagram of the electrical poling process by using an electrochemical cell. (g) Scheme of the uniphotocatalytic cell system for photocatalytic water splitting over the positively polarized $\text{CdS}/\text{Au}/\text{Ti}/\text{PMN-PT}$. (h) The hydrogen yield of the poled and unpoled samples without applying external voltage. Adapted with permission from Ref [55]. Copyright 2018 Elsevier. (i) Schematic illustrating the construction of the Z-schematic $\text{BiVO}_4\text{-BiFeO}_3\text{-CuInS}_2$ junction by anodic electrical poling process. Adapted with permission from Ref [56]. Copyright 2017 Elsevier.

It has been recognized that the ferroelectric polarization and screening effect can lead to the domain-dependent adsorption patterns of ferroelectric semiconductors, providing an effective tactic to modulate the adsorption of specific reactants.^[57] Li et al. utilized atomic force microscopy (AFM) and scanning surface

potential microscopy (SSPM) to investigate the ferroelectric-domain-dependent CO_2 adsorption on the surface of BaTiO_3 .^[58] The positively and negatively poled BaTiO_3 possessed the c^+ domain (dark area) and c^- domain (bright area), respectively, because of the opposite polarized charges on the surface (Figure 9a). The surface potential of BaTiO_3 after exposure to 30 L of CO_2 decreased with the chemisorption of CO_2 (Figure 9b). With increasing the doses of CO_2 , the average surface potentials of both c^+ and c^- domains initially decreased linearly and then remained unchanged as a result of saturated coverage of CO_2 (Figure 9c). The different decay trends of surface potential on the two opposite domains demonstrated the ferroelectric-domain-dependent CO_2 adsorption of BaTiO_3 . To further determine the CO_2 coverage difference of c^+ and c^- domains, the reactive sticking coefficient S (the ratio of chemisorbed molecules) was calculated by Equation (1):

$$\frac{\theta(L)}{\theta_{max}} = \frac{SL}{\theta_{max}N_0\sqrt{2\pi mk_bT}} \quad (1)$$

where the coverage θ is the fraction of the occupied sites per unit area, N_0 . When the exposure dose of an ideal gas is L , the number of impinging molecules can be represented as $L/\sqrt{2\pi mk_bT}$. Therefore, the reactive sticking coefficient S is proportional to the slope of the line in Figure 9d, which plotted the CO_2 coverage as a function of dosing $\theta(L)$. The slope ratio of c^- to c^+ reached 3.7 for BaTiO_3 , illustrating a better CO_2 adsorption on the negatively poled surface. Remarkably, the ferroelectric polarization-dependent molecule adsorption was mainly attributed to the anisotropic Van der Waals interactions between the adsorbates and polar surfaces, which reduced the activation barrier for physisorption while the chemisorption energy maintained unchanged.^[57] It has been reported that many alcohols with a low molecular weight, such as methanol, ethanol and 2-propanol, also have the polarization-dependent adsorption features.^[59] The charged dye molecules can also be effectively captured by the polar surfaces, resulting in an efficient decolorization process. Yin et al. reported the ferroelectric external screening effect of $\text{Bi}_3\text{TiNbO}_9$ for enhanced dye adsorption.^[60] After enhancing the polarization by corona poling, a giant external screening effect was generated for adsorbing a large amount of charged dyes on the polar surfaces to compensate the polarized charges (Figure 9e). The improved dye adsorption resulted in better photodegradation and photosensitization degradation performance of $\text{Bi}_3\text{TiNbO}_9$.

Recently, it has been reported that the photons with energy smaller than the band gap still excited electrons to transit to the CB, which can be possibly attributed to the ferroelectric polarization.^[61] Zhao et al. disentangled the relationship of ferroelectric polarization and optical absorption by theoretical calculation. Strengthening ferroelectric polarization effectively improved the optical absorption of the germanium iodide perovskite $\text{CH}_3\text{NH}_3\text{GeI}_3$ owing to the increased p-p orbital transition from I to Ge.^[62] Moreover, Liu et al. demonstrated that the charged domain walls in $\text{CH}_3\text{NH}_3\text{PbI}_3$ significantly reduced the band gap by providing an electric field across the domain.^[62b]

The above works uncover the great potential of ferroelectric polarization in promoting the crucial steps that occur in the photocatalytic process, including optical absorption, charge separation and adsorption of reactants. In particular, the electric poling by external electric field further enhances these advantages.

REVIEW

WILEY-VCH

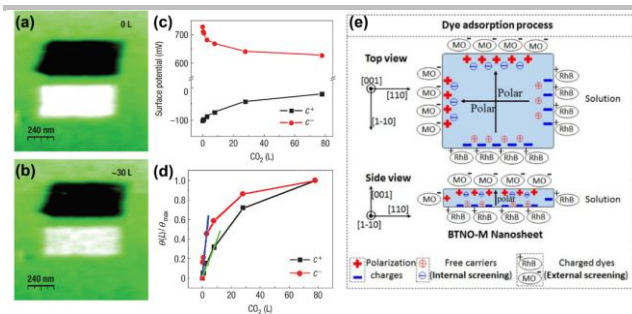


Figure 9. Surface potential maps of c^+ (dark region) and c^- domains (bright region) on BaTiO_3 (001) when exposure to (a) 0 L and (b) 30 L of CO_2 . (c) Average surface potential versus CO_2 dose on BaTiO_3 (001). (d) The computed reactive sticking coefficient of c^+ and c^- domains on BaTiO_3 (001). Adapted with permission from Ref [58]. Copyright 2008, Nature Publishing Group. (e) The dye adsorption process diagram of $\text{Bi}_3\text{TiNbO}_9$ single-crystal nanosheets. Adapted with permission from Ref [60]. Copyright 2020 Royal Society of Chemistry.

6. Magnetic field

Since the Zeeman effect of energy splitting in an external magnetic field was discovered in 1896, many researchers attempted to introduce the magnetic field into chemical reaction processes. It has been reported that the magnetic field can affect the free radical reactions, which includes the lifetime of free radicals and reaction intermediates.^[63] However, the Zeeman energy is not enough to alter the band structures of semiconductors. So the enhancement of photocatalytic performance by magnetic field is still a challenge. The Lorentz force induced by magnetic field can act as a driving force to facilitate the separation of photogenerated carriers and to promote the adsorption of ions on the catalysts' surface, leading to an improved photocatalytic activity under magnetic effect (Figure 10).

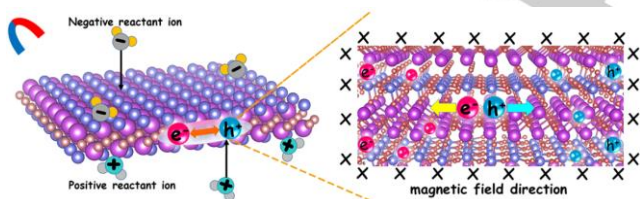


Figure 10. Schematic illustration for the magnetic field improved charge separation and adsorption of reactants.

The magnetically promoted photocatalytic reaction of ultrafine TiO_2 was initially found by Wakasa et al., and they interpreted it as the inhibited recombination of photoinduced electrons and holes in the semiconductors.^[64] After that, the introduction of magnetic field into photocatalytic processes mainly focused on improving the charge separation efficiency in semiconductors. The relative motion of charges in a magnetic field will generate Lorentz forces to deviate the charge movement. Thus, the separation and transfer of photogenerated carriers in the photocatalytic process can be effectively modulated by the magnetic field. For instance, Gao et al. investigated the functions of the magnetic field on the photocatalytic performance of TiO_2 nanobelts.^[11] The magnetic field induced Lorentz forces separated the electrons and holes to opposite directions, which

suppressed the charge recombination in bulk and allowed more active charge carriers to transfer to the surface. As a result, a 26% improvement of photocatalytic efficiency was achieved by simply incorporating the magnetic field in the photocatalytic system. They also discovered that the magnetic field can induce micro-electric potential in metal, which remarkably enhanced the charge separation in CdS by fabricating Au/CdS core-shell hybrid nanostructure.^[65] In order to cut the magnetic induction line during the movement of photocatalysts, a rotating permanent magnetic field was applied to the photocatalytic H_2 production system (Figure 11a). The introduction of magnetic field enhanced the H_2 production amount of Au/CdS by 110%, reaching an evolution rate of $222.8 \mu\text{mol}\cdot\text{g}^{-1}\cdot\text{h}^{-1}$ (Figure 11b). The polarized electrons in Au core along the direction of the Lorentz force under magnetic field produced surface charges at the interface between the core and shell, resulting in the formation of a space electric field, which facilitated the separation of photoinduced carriers in CdS shell (Figure 11c).

Magnetoresistance (MR) effect that the resistance of semiconductors varies with the applied magnetic field can be employed to tune the charge transport properties. Li et al. attributed the improved photocatalytic performance of $\alpha\text{-Fe}_2\text{O}_3/\text{rGO}$ to the negative MR effect that accelerated the transfer of photogenerated carriers at the interface.^[66] The increased photocurrent density and extended lifetime of photogenerated electrons under 1 kOe magnetic field evidenced the rapid separation and migration of photoinduced carriers (Figure 11d and 11e). Hence, the negative MR effect of both $\alpha\text{-Fe}_2\text{O}_3$ and rGO produced by the parallel alignment of magnetic moments increased the injection rates of electrons from $\alpha\text{-Fe}_2\text{O}_3$ to rGO, resulting in the transfer of more active carriers onto surface for redox reactions (Figure 11f).

Furthermore, the Lorentz force generated by magnetic field can also drive the reactants to be adsorbed on the surfaces of photocatalysts, which has the potential to break the limitation of adsorption quantity determined by intraparticle diffusion. For instance, the efficient photocatalytic denitrification of nitrate and ammonia was realized by $\text{Mn}_2\text{O}_3/\text{g-C}_3\text{N}_4$ with the assistance of magnetic field.^[67] The driving force produced by extra magnetic field not only promoted the separation of photoinduced electron-hole pairs in the heterojunctions, but also simultaneously enhanced the adsorption of the oppositely-charged NO_3^- -N and NH_4^+ -N by increasing their collision probability with $\text{Mn}_2\text{O}_3/\text{g-C}_3\text{N}_4$. In another study, Li et al. also reported the improved phosphorus adsorption on $\text{Fe}_3\text{O}_4/\text{ZnO}$ magnetic composites via the weak magnetic effect.^[67b]

Therefore, introducing the magnetic field into photocatalytic processes is an effective and practical approach to enhance the solar energy conversion efficiency with the improved charge separation and surface adsorption. More examples of the external fields improved photocatalytic reactions are summarized in Table 1.

REVIEW

WILEY-VCH

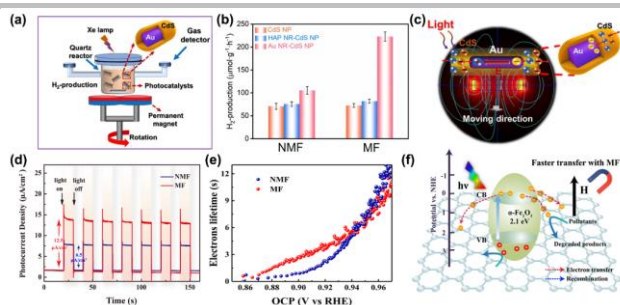


Figure 11. (a) Schematic illustration of the photocatalytic H_2 production system under magnetic field. (b) Photocatalytic H_2 production rates of Au NR-CdS NP core-shell with no magnetic field (NMF) or with a magnetic field (MF). (c) Schematic illustrating the carrier separation of the moving Au NR-CdS NP core-shell nanostructure under a magnetic field. Adapted with permission from Ref [65]. Copyright 2020 Elsevier. (d) The transient photocurrent density of $\alpha\text{-Fe}_2\text{O}_3/\text{rGO}$ with or without magnetic field. (e) Electron lifetime as a function of open-circuit potential with or without magnetic field. (f) Schematic illustrating the transfer of carriers in the $\alpha\text{-Fe}_2\text{O}_3/\text{rGO}$ with the large negative magnetoresistance effect under light and magnetic fields. Adapted with permission from Ref [66]. Copyright 2018 American Chemical Society.

Table 1. Typical examples for external fields improved photocatalytic performance.

Photocatalysts	Catalytic conditions	Catalytic applications	Catalytic efficiency or rate	Ref.
F/Si/TiO ₂	Two electrodeless discharge lamps	Degradation of pentachlorophenol (c = 40 mg·L ⁻¹)	99% degradation efficiency within 20 min	[68]
TiO ₂ /CNT	Microwave electrodeless discharge lamps	Degradation of atrazine (c = 20 mg·L ⁻¹)	100% degradation efficiency within 3 min	[69]
P25	Electrodeless discharge lamps + H ₂ O ₂ (0.1% v/v)	Degradation of 4-CP (c = 30 mg·L ⁻¹)	k = ~ 0.0192 min ⁻¹	[70]
ZnO/CuO	Xenon lamp (300 W) + microwave (1.5 W)	Degradation of tetanus toxin (c = 1 mg·L ⁻¹)	k = ~ 0.0652 min ⁻¹	[71]
BiFeO ₃ nanowires	Xenon lamp (300 W) + ultrasonic (80 W, 132 kHz)	Degradation of RhB (c = 4 mg·L ⁻¹)	k = 0.0582 min ⁻¹	[72]
KNbO ₃ nanosheets	Xenon lamp (300 W) + ultrasonic (110 W, 40 kHz)	Degradation of RhB (c = 10 mg·L ⁻¹)	k = 0.0220 min ⁻¹	[30b]
MoS ₂ /KNbO ₃	Xenon lamp (300 W) + ultrasonic (110 W, 40 kHz)	Degradation of RhB (c = 10 mg·L ⁻¹)	k = 0.0370 min ⁻¹	[73]
ZnO nanorods	UV light (24 W) + ultrasonic (150 W, 40 kHz)	Degradation of AO7 (c = 10 mg·L ⁻¹)	k = 0.0173 min ⁻¹	[74]
ZnO nanowire array on PDMS	UV light (9 W) + stirring	Degradation of MB (c = 10 mM)	k = 0.0091 min ⁻¹	[74b]
Au/ZnO	Xenon lamp (300 W) + ultrasonic (80 W, 40 kHz)	Degradation of RhB (c = 5 mg·L ⁻¹)	k = ~ 0.0399 min ⁻¹	[74c]
Cl/ZnO nanorods	Xenon lamp (300 W) + ultrasonic (100 W, 40 kHz)	Degradation of RhB (c = 10 ppm, 50 mL)	k = 0.0232 min ⁻¹	[74d]
BaTiO ₃ nanowires	UV-LED (4.2 W) + ultrasonic (180 W, 40 kHz)	Degradation of MO (c = 5 mg·L ⁻¹)	k = 0.0426 min ⁻¹	[75]
Ag/BaTiO ₃	Xenon lamp (300 W) + ultrasonic	Degradation of RhB (c = 0.01 mM)	k = ~ 0.0236 min ⁻¹	[75b]
Ag ₂ O/BaTiO ₃	Xenon lamp + ultrasonic (50 W, 40 kHz)	Degradation of RhB (c = 15 mg·L ⁻¹)	k = 0.0510 min ⁻¹	[75c]
Al/BaTiO ₃	Xenon lamp (300 W) + ultrasonic	H ₂ evolution	327 μmol·g ⁻¹ ·cm ⁻²	[75d]
CdS nanorod arrays	Xenon lamp (300 W) + ultrasonic (100W, 27 kHz)	H ₂ evolution	20 μL·h ⁻¹	[76]
MoS ₂ /Ag ₂ O	Infrared lamp (300 W) + ultrasonic	Degradation of MO (c = 20 mg·L ⁻¹)	k = ~ 0.0803 min ⁻¹	[76b]
PMN-PT/TiO ₂	UV light (15W) + ultrasonic (180 W, 53 kHz)	Degradation of RhB (c = 12 mg·L ⁻¹)	k = ~ 0.0219 min ⁻¹	[77]
PVDF/TiO ₂	UV lamp + air bubble	Degradation of MB (c = 0.01 μM)	100% degradation efficiency within 90 min	[39c]
PVDF/ZnO	Xenon lamp (300 W) + stirring	Degradation of RhB (c = 12 mg·L ⁻¹)	k = 0.0391 min ⁻¹	[39b]
ZnS:Cu	Xenon lamp (500 W) + thermal cycling	Degradation of AO7 (c = 5 mg·L ⁻¹)	k = ~ 0.0499 min ⁻¹	[46b]
Au/Bi ₆ Fe ₂ Ti ₃ O ₁₈	Corona poling + fluorescent lamp (20 W)	Degradation of RhB	k = ~ 0.0154 min ⁻¹	[78]
Ba _{0.875} Ca _{0.125} Ti _{0.95} Sn _{0.05} O _{3-δ} -Sn	Corona poling + solar simulator (375 nm)	Degradation of MB (c = 5 mg·L ⁻¹)	k = ~ 0.0368 min ⁻¹	[79]
g-C ₃ N ₄ /BaTiO ₃	Electric poling + UV/vis light	Degradation of MO	k = ~ 0.0065 min ⁻¹	[80]

C ₃ N ₄ /BiFeO ₃	Electric poling + xenon lamp (500 W)	Degradation of RhB (c = 10 mg·L ⁻¹)	100% degradation efficiency within 80 min	[80b]
KNbO ₃	Electric poling + UV light	Degradation of RhB (c = 10 mg·L ⁻¹)	k = 0.3170 min ⁻¹	[81]
BiOI/Bi ₄ Ti ₃ O ₁₂	Electric poling + UV light	Degradation of RhB (c = 10 mg·L ⁻¹)	100% degradation efficiency within 12 min	[82]
ZnO	UV light + magnetic field (0.7 T)	Degradation of MB (c = 0.02 mM)	k = ~ 0.0108 min ⁻¹	[83]
TiO ₂	UV light + magnetic field (100Oe)	Degradation of MO (c = 5 μM)	k = ~ 0.0017 min ⁻¹	[84]
Fe ₃ O ₄ /TiO ₂	UV/Vis light + magnetic field (800 Oe)	Degradation of RhB (c = 0.1 mM)	k = 0.2140 min ⁻¹	[85]
P25 and Fe ₃ O ₄	UV light (120 W) + magnetic field (15 mT) + sound pressure (100 Hz)	Degradation of formaldehyde (20 mg/m ³)	k = ~ 0.0183 min ⁻¹	[86]
CoFe ₂ O ₄ /MoS ₂	Xenon lamp (300 W) + magnetic field (1500 Oe)	Degradation of Congo red (c = 20 mg·L ⁻¹)	k = ~ 0.0457 min ⁻¹	[87]

7. Multi-external fields

The synergy of the multiple external fields shows a great potential to significantly improve the solar-to-chemical energy conversion efficiency. It mainly involves the ferro/piezo/pyro-phototronic effects of the polar materials, of which the coupled external stimulations induce a stronger polarization for drastically promoting the separation and transport of photoinduced charge carriers.^[88] It is well known that ferroelectrics possess both piezoelectric and pyroelectric properties intrinsically. Even for electrically poled ferroelectrics, they only have remnant polarization with inconsistently-arranged domains. With the applied external strain or temperature fluctuation, the domains may be well aligned by the as-introduced piezo- or pyro-potential, which enhances the polarization of ferroelectrics and thereby results in the promoted charge separation. Thus, the photocatalytic reactions of ferroelectric semiconductors can be dramatically advanced by combining the mechanical stress or temperature gradient fields with electric poling, realizing the ferro/piezo-photocatalysis or ferro/pyro-photocatalysis (Figure 12).

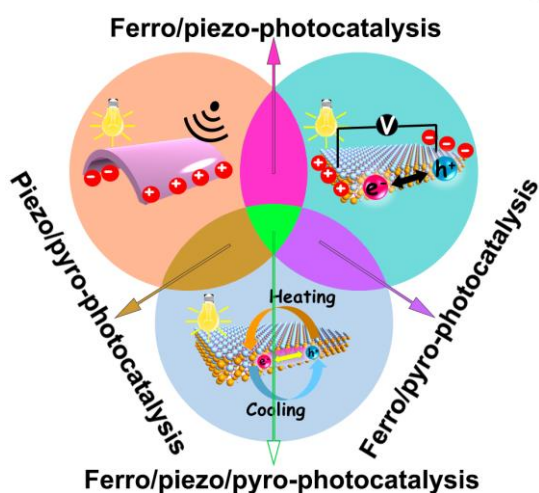


Figure 12. Schematic illustration for the multi-fields coupled photocatalysis

For instance, BiFeO₃/TiO₂ core-shell nanocomposites were constructed and polarized to decompose the dye molecules under ultrasonic and light irradiation; the piezo-photocatalytic degradation performance of poled BiFeO₃/TiO₂ was remarkably

enhanced, over 235% increase compared to that of the untreated counterpart. The coupling effect of ferroelectric and piezoelectric polarization generated a steeper band bending at the heterostructure interface that facilitated the separation of electrons and holes.^[89] In other applications, Kumar et al. achieved 100% piezo-photocatalytic bacterial inactivation using the poled BaTiO₃ (BTO) ceramic within 30 min. As we know, the ROS have a lethal effect on bacterial survival. The improved photoinduced charge separation by surface polarization can produce a sufficiently high voltage to trigger the rapid generation of ROS under mechanical vibration and UV irradiation (Figure 13a).^[90] Similarly, the poled TiO₂/BTO/Au nanorod arrays exhibited an efficient photodynamic bacteria killing performance by coupling the ferro/piezophototronic and SPR effects. The piezopotential and remnant polarization enhanced the charge transport at the interface of the ternary heterojunction, rendering a large number of ROS.^[90b] Moreover, the electric poling process remarkably enhanced the fluid-driven piezo-photocatalytic performance of PbTiO₃ monocrystalline nanoplates because of the synergistic advantages of piezoelectric and ferroelectric polarization.^[91]

The pyro-phototronic effect can be utilized to enhance the photocurrent density of pyroelectric semiconductors. However, most of them possessed an unsatisfied thermoelectric conversion efficiency. It has been reported that the pyroelectric coefficient of poled ferroelectric BaTiO₃ reached 16 nC/cm²K, which could enhance the pyro-phototronic effect to yield a considerable current output.^[92] With a cooling temperature variation, the stable current plateau of the BaTiO₃ device composed of a BaTiO₃ layer sandwiched between two ITO glass was enhanced by 23% due to the band bending induced by ferro-pyro-phototronic effect. The increased polarized charges induced a downward band bending at the positive side to reduce the Schottky barrier height, which promoted the electron flow to the right ITO electrode. Meanwhile, the upward band bending at the negative side further separated the photoexcited electron-hole pairs with the increased Schottky barrier height on the left (Figure 13b).

The mechanical stress and temperature gradient fields can also be integrated into the photocatalytic process, highlighting the piezo/pyro-photocatalysis (Figure 12). In a typical case, Ag₂O/BaTiO₃ composites were prepared to take advantage of the photocatalytic properties of Ag₂O, piezoelectricity and pyroelectricity of BaTiO₃ for efficient piezo/pyro-photocatalytic degradation of MO under the varied temperature field and ultrasonic excitation (Figure 13c).^[93] The decolorization activity of Ag₂O/BaTiO₃ via the piezo/pyro-photocatalytic process reached a rate of 0.020 min⁻¹, which is 1.4 and 1.3 times faster

REVIEW

WILEY-VCH

than that of the photocatalysis (0.015 min^{-1}) and pyro-photocatalysis (0.016 min^{-1}), respectively. The piezoelectric and pyroelectric bound charges formed in BaTiO_3 attracted and released photoexcited charge carriers during the temperature fluctuation and ultrasonic vibration cycling, which dramatically improved the charge separation efficiency and surface redox reactions (Figure 13d).

Multi-external fields can result in much stronger polarization, which provides a more powerful driving force for charge separation. In view of the great enhancement of photocatalytic performance by the coupling effects derived from multi-external fields, this strategy is expected to show huge prospect in photocatalytic applications.

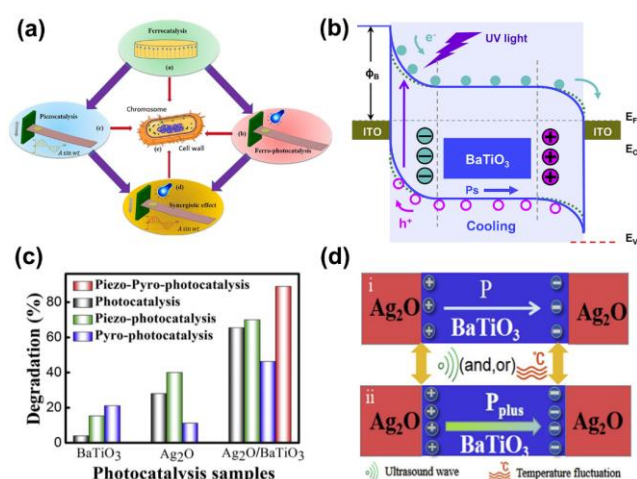


Figure 13. (a) Schematic illustration for the bacterial inactivation process by ferro/piezophotocatalysis. Adapted with permission from Ref [90]. Copyright 2019 Elsevier. (b) Schematic illustration for the band bending of the poled BaTiO_3 device with a cooling temperature variation. Adapted with permission from Ref [92]. Copyright 2018 Elsevier. (c) Piezo/pyro-photocatalytic MO degradation performance over $\text{Ag}_2\text{O}/\text{BaTiO}_3$. (d) Schematic diagram of the piezo/pyro-photocatalytic degradation process over $\text{Ag}_2\text{O}/\text{BaTiO}_3$ composite. Adapted with permission from Ref [93]. Copyright 2020 Elsevier.

8. Summary and Outlook

Efficient conversion of solar energy through photocatalytic processes is a prospective approach to relieve energy crisis and environmental pollution, known as the “21st Century Dream Technology”. However, the low catalytic efficiency is still far behind the practical application requirement. Introduction of external fields provides a straightforward and effective strategy to improve the photocatalytic performance of semiconductors. In this review, we summarized the advances on utilization of diverse external fields, including the microwave, mechanical stress, temperature gradient, external electric field, magnetic field and coupled-fields, to boost the photocatalytic activity for various reactions, such as water splitting, CO_2 reduction, bacterial inactivation and pollutant degradation. The mechanisms for photo-reactivity reinforcement associated with the improved photoabsorption, charge separation, surface adsorption and activation were discussed. Though the external field assisted photocatalytic processes can largely overcome the instinct weakness of the photocatalysts, there are still some fundamental issues and challenges need to be conquered.

i) The improvement of photocatalytic efficiency by the external fields is still restricted by low utilization of external energy

injected into the photocatalytic reaction system, as the dominating factors that the external fields enhance the photocatalytic performance of semiconductors has not been clarified enough. It was demonstrated that the synergy between the external fields and internal electric fields in hybrid semiconductors significantly improved the photocatalytic performance. Thus, more efforts should be made to explore the influence of material modifications, such as defects formation, fabrication of ultra-small or ultra-thin structures, etc., on external fields to maximumly take advantages of external energy. Besides, more forms of energy existed in the natural environment are anticipated to be exploited as the source of external fields, such as wind energy, tidal energy, and geothermal energy, etc.

ii) The development of highly polar photocatalysts (ferro/piezo/pyro-electrics) is urgently needed, since they are more sensitive to the applied external fields. Their non-centrosymmetric structures can generate a strong polarization as driving force to boost the separation and transfer of photoactivated charge carriers when an external field was applied. Some tactics for material design, such as elemental substitution, microstructure modulation and surface decoration, may show large potential to enhance the polarization strengthen of polar materials, which can be employed to assist the external field assisted photocatalytic processes.

iii) Coupling of multiple external fields shows huge prospects as it may produce synergistic effect to substantially increase the photocatalytic efficiency. However, the different external fields may produce the potential on photocatalysts or effects on photocatalysis against each other, which cripples the photocatalytic performance. Therefore, in-depth understanding on the coupling mechanism and rational optimization of the parameters of diverse external fields is indispensable to achieve efficient photocatalytic reactions.

iv) Until now, most of photocatalytic reactions enhanced by external fields are mainly concentrated on contaminants removal, and only a spot of works involve H_2 evolution and CO_2 reduction. The applications for generation of solar fuel should be deepened. Particularly, it is promising to extend the application scope of external field enhanced photocatalysis to other reactions, such as N_2 fixation and organic synthesis.

v) More in situ characterization techniques should be developed to further probe the functions of external fields in photocatalytic processes, for instance, the processes of charge generation and separation in bulk, adsorption processes of reactant molecules on the surface of semiconductors. These in situ measurements are conducive to identifying the behaviors of carriers and reactant molecules under the external fields, as well as the evolution of structures and properties of the catalysts. Besides, as some external fields play a part by inducing the establishing of internal electric fields, the characterization techniques for internal fields, such as light-assisted Kelvin probe force microscopy and surface photovoltage microscopy, are in need.

Acknowledgements

This work was jointly supported by the National Natural Science Foundation of China (No. 51972288 and 51672258), the Fundamental Research Funds for the Central Universities (2652018287).

REVIEW

WILEY-VCH

Keywords: external fields • photocatalysis • charge separation • polar materials

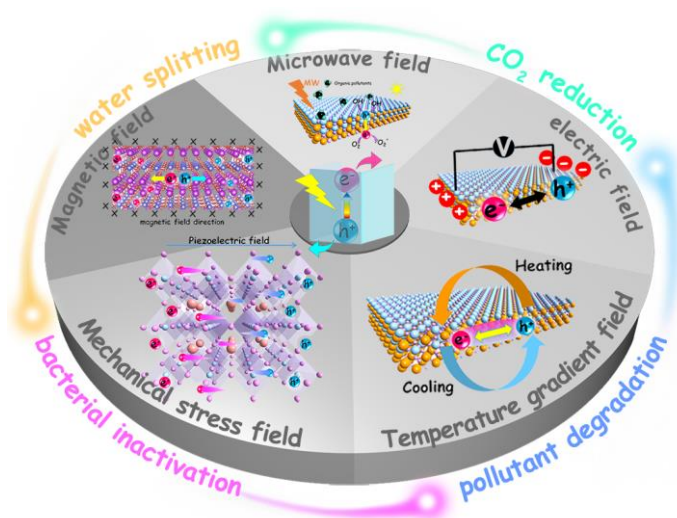
- [1] a) J. Schneider, M. Matsuoka, M. Takeuchi, J. Zhang, Y. Horiuchi, M. Anpo, D. W. Bahnemann, *Chem. Rev.* **2014**, *114*, 9919-9986; b) J. C. Colmenares, R. Luque, *Chem. Soc. Rev.* **2014**, *43*, 765-778; c) X. Chen, S. Shen, L. Guo, S. S. Mao, *Chem. Rev.* **2010**, *110*, 6503-6570.
- [2] S. Bai, J. Jiang, Q. Zhang, Y. Xiong, *Chem. Soc. Rev.* **2015**, *44*, 2893-2939.
- [3] Q. Zeng, H. Wang, W. Fu, Y. Gong, W. Zhou, P. M. Ajayan, J. Lou, Z. Liu, *Small* **2015**, *11*, 1868-1884.
- [4] a) Y. Liu, S. Ye, H. Xie, J. Zhu, Q. Shi, N. Ta, R. Chen, Y. Gao, H. An, W. Nie, H. Jing, F. Fan, C. Li, *Adv. Mater.* **2020**, *32*, 1906513; b) J. Li, L. Cai, J. Shang, Y. Yu, L. Zhang, *Adv. Mater.* **2016**, *28*, 4059-4064.
- [5] a) L. Hao, L. Kang, H. Huang, L. Ye, K. Han, S. Yang, H. Yu, M. Batmunkh, Y. Zhang, T. Ma, *Adv. Mater.* **2019**, *31*, 1900546; b) H. Yu, J. Li, Y. Zhang, S. Yang, K. Han, F. Dong, T. Ma, H. Huang, *Angew. Chem. Int. Ed.* **2019**, *58*, 3880-3884.
- [6] X. Wang, W. Gao, Z. Zhao, L. Zhao, J. P. Claverie, X. Zhang, J. Wang, H. Liu, Y. Sang, *Appl. Catal., B* **2019**, *248*, 388-393.
- [7] S. Wang, G. Liu, L. Wang, *Chem. Rev.* **2019**, *119*, 5192-5247.
- [8] a) H. You, Y. Jia, Z. Wu, F. Wang, H. Huang, Y. Wang, *Nat. Commun.* **2018**, *9*, 2889; b) H. Huang, S. Tu, C. Zeng, T. Zhang, A. H. Reshak, Y. Zhang, *Angew. Chem. Int. Ed.* **2017**, *56*, 11860-11864; c) L. T. Tufa, K.-J. Jeong, V. T. Tran, J. Lee, *ACS Appl. Mater. Interfaces* **2020**, *12*, 6598-6606.
- [9] S. Horikoshi, H. Hidaka, N. Serpone, *Environ. Sci. Technol.* **2002**, *36*, 1357-1366.
- [10] F. Chen, H. Huang, L. Guo, Y. Zhang, T. Ma, *Angew. Chem. Int. Ed.* **2019**, *58*, 10061-10073.
- [11] W. Gao, J. Lu, S. Zhang, X. Zhang, Z. Wang, W. Qin, J. Wang, W. Zhou, H. Liu, Y. Sang, *Adv. Sci.* **2019**, *6*, 1901244.
- [12] A. Kakekhan, S. Ismail-Beigi, E. I. Altman, *Surf. Sci.* **2016**, *650*, 302-316.
- [13] L. Pan, S. Sun, Y. Chen, P. Wang, J. Wang, X. Zhang, J.-J. Zou, Z. L. Wang, *Adv. Energy Mater.* **2020**, *10*, 2000214.
- [14] M. Wang, B. Wang, F. Huang, Z. Lin, *Angew. Chem. Int. Ed.* **2019**, *58*, 7526-7536.
- [15] S. Li, Z. Zhao, J. Zhao, Z. Zhang, X. Li, J. Zhang, *ACS Appl. Nano Mater.* **2020**, *3*, 1063-1079.
- [16] S. Horikoshi, M. Abe, N. Serpone, *Photochem. Photobiol. Sci.* **2009**, *8*, 1087-1104.
- [17] A. A. Amer, S. M. Reda, M. A. Mousa, M. M. Mohamed, *RSC Adv.* **2017**, *7*, 826-839.
- [18] V. Nair, M. J. Muñoz-Batista, M. Fernández-García, R. Luque, J. C. Colmenares, *ChemSusChem* **2019**, *12*, 2098-2116.
- [19] a) S. Horikoshi, Y. Minatodani, H. Tsutsumi, H. Uchida, M. Abe, N. Serpone, *J. Photochem. Photobiol. A: Chem.* **2013**, *265*, 20-28; b) Z. Ai, P. Yang, X. Lu, *J. Hazard. Mater.* **2005**, *124*, 147-152.
- [20] S. Horikoshi, A. Matsubara, S. Takayama, M. Sato, F. Sakai, M. Kajitani, M. Abe, N. Serpone, *Appl. Catal., B* **2009**, *91*, 362-367.
- [21] S. Horikoshi, F. Sakai, M. Kajitani, M. Abe, A. V. Emeline, N. Serpone, *J. Phys. Chem. C* **2009**, *113*, 5649-5657.
- [22] S. Horikoshi, H. Tsutsumi, H. Matsuzaki, A. Furube, A. V. Emeline, N. Serpone, *J. Mater. Chem. C* **2015**, *3*, 5958-5969.
- [23] S. Horikoshi, H. Hidaka, N. Serpone, *Chem. Phys. Lett.* **2003**, *376*, 475-480.
- [24] S. Horikoshi, A. Saitou, H. Hidaka, N. Serpone, *Environ. Sci. Technol.* **2003**, *37*, 5813-5822.
- [25] L. Ling, Y. Feng, H. Li, Y. Chen, J. Wen, J. Zhu, Z. Bian, *Appl. Surf. Sci.* **2019**, *483*, 772-778.
- [26] a) A. J. Barik, S. V. Kulkarni, P. R. Gogate, *Sep. Purif. Technol.* **2016**, *168*, 152-160; b) U. Riaz, J. Zia, *Environ. Pollut.* **2020**, *259*, 113917; c) S. J. Ki, K.-J. Jeon, Y.-K. Park, S. Jeong, H. Lee, S.-C. Jung, *Catal. Today* **2017**, *293-294*, 15-22; d) J. Hong, C. Sun, S.-G. Yang, Y.-Z. Liu, *J. Hazard. Mater.* **2006**, *133*, 162-166; e) G. Zhanqi, Y. Shaogui, T. Lee, S. Cheng, *J. Hazard. Mater.* **2007**, *145*, 424-430; f) S. Jeong, H. Lee, N. H. Park, K.-J. Jeon, Y.-K. Park, S.-C. Jung, *Catal. Today* **2018**, *307*, 65-72; g) H. Lee, S. H. Park, Y.-K. Park, S.-J. Kim, S.-G. Seo, S. J. Ki, S.-C. Jung, *Chem. Eng. J.* **2015**, *278*, 259-264.
- [27] Q. Yang, X. Guo, W. Wang, Y. Zhang, S. Xu, D. H. Lien, Z. L. Wang, *ACS Nano* **2010**, *4*, 6285-6291.
- [28] S. Bai, L. Wang, Z. Li, Y. Xiong, *Adv. Sci.* **2017**, *4*, 1600216.
- [29] Z. Liang, C.-F. Yan, S. Rtimi, J. Bandara, *Appl. Catal., B* **2019**, *241*, 256-269.
- [30] a) J. Wu, N. Qin, D. Bao, *Nano Energy* **2018**, *45*, 44-51; b) D. Yu, Z. Liu, J. Zhang, S. Li, Z. Zhao, L. Zhu, W. Liu, Y. Lin, H. Liu, Z. Zhang, *Nano Energy* **2019**, *58*, 695-705.
- [31] Y. Zhao, X. Huang, F. Gao, L. Zhang, Q. Tian, Z.-B. Fang, P. Liu, *Nanoscale* **2019**, *11*, 9085-9090.
- [32] S. Singh, N. Khare, *Nano Energy* **2017**, *38*, 335-341.
- [33] Y.-C. Wang, J. M. Wu, *Adv. Funct. Mater.* **2020**, *30*, 1907619.
- [34] C. Hu, H. Huang, F. Chen, Y. Zhang, H. Yu, T. Ma, *Adv. Funct. Mater.* **2020**, *30*, 1908168.
- [35] a) X. Zhou, F. Yan, S. Wu, B. Shen, H. Zeng, J. Zhai, *Small* **2020**, *16*, 2001573; b) X. Zhou, S. Wu, C. Li, F. Yan, H. Bai, B. Shen, H. Zeng, J. Zhai, *Nano Energy* **2019**, *66*, 104127.
- [36] S. Xu, L. Guo, Q. Sun, Z. L. Wang, *Adv. Funct. Mater.* **2019**, *29*, 1808737.
- [37] a) D. Hong, W. Zang, X. Guo, Y. Fu, H. He, J. Sun, L. Xing, B. Liu, X. Xue, *ACS Appl. Mater. Interfaces* **2016**, *8*, 21302-21314; b) Z. Wang, T. Hu, H. He, Y. Fu, X. Zhang, J. Sun, L. Xing, B. Liu, Y. Zhang, X. Xue, *ACS Sustainable Chem. Eng.* **2018**, *6*, 10162-10172.
- [38] Y. Feng, L. Ling, Y. Wang, Z. Xu, F. Cao, H. Li, Z. Bian, *Nano Energy* **2017**, *40*, 481-486.
- [39] a) W. Tong, Y. Zhang, H. Huang, K. Xiao, S. Yu, Y. Zhou, L. Liu, H. Li, L. Liu, T. Huang, M. Li, Q. Zhang, R. Du, Q. An, *Nano Energy* **2018**, *53*, 513-523; b) W. Wu, X. Yin, B. Dai, J. Kou, Y. Ni, C. Lu, *Appl. Surf. Sci.* **2020**, *517*, 146119; c) A. Durairaj, S. Ramasundaram, T. Sakthivel, S. Ramanathan, A. Rahaman, B. Kim, S. Vasanthkumar, *Appl. Surf. Sci.* **2019**, *493*, 1268-1277.
- [40] Y. Feng, H. Li, L. Ling, S. Yan, D. Pan, H. Ge, H. Li, Z. Bian, *Environ. Sci. Technol.* **2018**, *52*, 7842-7848.
- [41] Y. Chen, L. Wang, R. Gao, Y.-C. Zhang, L. Pan, C. Huang, K. Liu, X.-Y. Chang, X. Zhang, J.-J. Zou, *Appl. Catal., B* **2019**, *259*, 118079.
- [42] a) X. Xue, W. Zang, P. Deng, Q. Wang, L. Xing, Y. Zhang, Z. L. Wang, *Nano Energy* **2015**, *13*, 414-422; b) M. B. Starr, J. Shi, X. Wang, *Angew. Chem. Int. Ed.* **2012**, *51*, 5962-5966.
- [43] K. Zhang, Z. L. Wang, Y. Yang, *ACS Nano* **2016**, *10*, 10331-10338.
- [44] X. Xu, L. Xiao, Y. Jia, Z. Wu, F. Wang, Y. Wang, N. O. Haugen, H. Huang, *Energy Environ. Sci.* **2018**, *11*, 2198-2207.
- [45] a) Z. Wang, R. Yu, X. Wang, W. Wu, Z. L. Wang, *Adv. Mater.* **2016**, *28*, 6880-6886; b) Y. Dai, X. Wang, W. Peng, C. Xu, C. Wu, K. Dong, R. Liu, Z. L. Wang, *Adv. Mater.* **2018**, *30*, 1705893.
- [46] a) J. Chen, W. Luo, S. Yu, X. Yang, Z. Wu, H. Zhang, J. Gao, Y.-W. Mai, Y. Li, Y. Jia, *Ceram. Int.* **2020**, *46*, 9786-9793; b) W. Luo, J. Ying, S. Yu, X. Yang, Y. Jia, M. Chen, H. Zhang, J. Gao, Y. Li, Y.-W. Mai, Z. Wu, *Ceram. Int.* **2020**, *46*, 12096-12101; c) Y. Liu, X. Wang, Y. Qiao, M. Min, L. Wang, H. Shan, Y. Ma, W. Hao, P. Tao, W. Shang, J. Wu, C. Song, T. Deng, *ACS Sustainable Chem. Eng.* **2019**, *7*, 2602-2609.
- [47] a) M. Min, Y. Liu, C. Song, D. Zhao, X. Wang, Y. Qiao, R. Feng, W. Hao, P. Tao, W. Shang, J. Wu, T. Deng, *ACS Appl. Mater. Interfaces* **2018**, *10*, 21246-21253; b) B. Dai, J. Fang, Y. Yu, M. Sun, H. Huang, C. Lu, J. Kou, Y. Zhao, Z. Xu, *Adv. Mater.* **2020**, *32*, 1906361.
- [48] a) S. Tiewcharoen, C. Warakulwit, V. Lapeyre, P. Garrigue, L. Fourier, C. Elissalde, S. Buffière, P. Legros, M. Gayot, J. Limtrakul, A. Kuhn, *Angew. Chem. Int. Ed.* **2017**, *56*, 11431-11435; b) Y. Zhao, Z. Huang, W. Chang, C. Wei, X. Feng, L. Ma, X. Qi, Z. Li, *Chemosphere* **2017**, *179*, 75-83.
- [49] Y. Zhang, T.-T. Tang, C. Girit, Z. Hao, M. C. Martin, A. Zettl, M. F. Crommie, Y. R. Shen, F. Wang, *Nature* **2009**, *459*, 820-823.
- [50] J. Kim, S. S. Baik, S. H. Ryu, Y. Sohn, S. Park, B.-G. Park, J. Denlinger, Y. Yi, H. J. Choi, K. S. Kim, *Science* **2015**, *349*, 723.
- [51] a) C. Zhao, D. Huang, J. Chen, Y. Li, Z. Du, *RSC Adv.* **2016**, *6*, 98908-98915; b) C. M. Tank, Y. S. Sakhare, N. S. Kanhe, A. B. Nawale, A. K. Das, S. V. Bhoraskar, V. L. Mathe, *Solid State Sci.* **2011**, *13*, 1500-1504.
- [52] a) F. Ling, X. Liu, H. Jing, Y. Chen, W. Zeng, Y. Zhang, W. Kang, J. Liu, L. Fang, M. Zhou, *PCCP* **2018**, *20*, 26083-26090; b) M. Yan, X. Pan, P. Wang, F. Chen, L. He, G. Jiang, J. Wang, J. Z. Liu, X. Xu, X. Liao, J. Yang, L. Mai, *Nano Lett.* **2017**, *17*, 4109-4115; c) H. Guo, W. Zhang, N.

REVIEW

WILEY-VCH

- Lu, Z. Zhuo, X. C. Zeng, X. Wu, J. Yang, *J. Phys. Chem. C* **2015**, *119*, 6912-6917.
- [53] a) S. Park, C. W. Lee, M.-G. Kang, S. Kim, H. J. Kim, J. E. Kwon, S. Y. Park, C.-Y. Kang, K. S. Hong, K. T. Nam, *PCCP* **2014**, *16*, 10408-10413; b) S. Li, L. Bai, N. Ji, S. Yu, S. Lin, N. Tian, H. Huang, *J. Mater. Chem. A* **2020**, *8*, 9268-9277.
- [54] a) G. Zhang, J. Cao, G. Huang, J. Li, D. Li, W. Yao, T. Zeng, *Catal. Sci. Technol.* **2018**, *8*, 6420-6428; b) G. Huang, G. Zhang, Z. Gao, J. Cao, D. Li, H. Yun, T. Zeng, *J. Alloys Compd.* **2019**, *783*, 943-951.
- [55] Z. Song, B. Hong, X. Zhu, F. Zhang, S. Li, J. Ding, X. Jiang, J. Bao, C. Gao, S. Sun, *Appl. Catal., B* **2018**, *238*, 248-254.
- [56] H. Li, X. Quan, S. Chen, H. Yu, *Appl. Catal., B* **2017**, *209*, 591-599.
- [57] M. A. Khan, M. A. Nadeem, H. Idriss, *Surf. Sci. Rep.* **2016**, *71*, 1-31.
- [58] D. Li, M. H. Zhao, J. Garra, A. M. Kolpak, A. M. Rappe, D. A. Bonnelli, J. M. Vohs, *Nat. Mater.* **2008**, *7*, 473-477.
- [59] Y. Cui, J. Briscoe, S. Dunn, *Chem. Mater.* **2013**, *25*, 4215-4223.
- [60] X. Yin, Y. Sun, X. Wu, X. Li, H. Liu, W. Gu, W. Zou, L. Zhu, Z. Fu, Y. Lu, *Catal. Sci. Technol.* **2020**, *10*, 2864-2873.
- [61] C. C. Stoumpos, L. Frazer, D. J. Clark, Y. S. Kim, S. H. Rhim, A. J. Freeman, J. B. Ketterson, J. I. Jang, M. G. Kanatzidis, *J. Am. Chem. Soc.* **2015**, *137*, 6804-6819.
- [62] a) Y.-Q. Zhao, B. Liu, Z.-L. Yu, J. Ma, W. Qiang, P.-b. He, M.-Q. Cai, *J. Mater. Chem. C* **2017**, *5*, 5356-5364; b) S. Liu, F. Zheng, N. Z. Koocher, H. Takenaka, F. Wang, A. M. Rappe, *J. Phys. Chem. Lett.* **2015**, *6*, 693-699.
- [63] U. E. Steiner, T. Ulrich, *Chem. Rev.* **1989**, *89*, 51-147.
- [64] M. Wakasa, S. Suda, H. Hayashi, N. Ishii, M. Okano, *J. Phys. Chem. B* **2004**, *108*, 11882-11885.
- [65] W. Gao, Q. Liu, S. Zhang, Y. Yang, X. Zhang, H. Zhao, W. Qin, W. Zhou, X. Wang, H. Liu, Y. Sang, *Nano Energy* **2020**, *71*, 104624.
- [66] J. Li, Q. Pei, R. Wang, Y. Zhou, Z. Zhang, Q. Cao, D. Wang, W. Mi, Y. Du, *ACS Nano* **2018**, *12*, 3351-3359.
- [67] a) J. Zhao, N. Li, R. Yu, Z. Zhao, J. Nan, *Chem. Eng. J.* **2018**, *349*, 530-538; b) N. Li, Y. Tian, J. Zhao, W. Zhan, J. Du, L. Kong, J. Zhang, W. Zuo, *Chem. Eng. J.* **2018**, *341*, 289-297.
- [68] S. Yang, H. Fu, C. Sun, Z. Gao, *J. Hazard. Mater.* **2009**, *161*, 1281-1287.
- [69] H. Chen, S. Yang, K. Yu, Y. Ju, C. Sun, *J. Phys. Chem. A* **2011**, *115*, 3034-3041.
- [70] A. Zhihui, Y. Peng, L. Xiaohua, *Chemosphere* **2005**, *60*, 824-827.
- [71] A. Fakhri, M. Azad, L. Fatollahi, S. Tahami, *J. Photochem. Photobiol. B: Biol.* **2018**, *178*, 108-114.
- [72] F. Mushtaq, X. Chen, M. Hoop, H. Torlakcik, E. Pellicer, J. Sort, C. Gattinoni, B. J. Nelson, S. Pané, *iScience* **2018**, *4*, 236-246.
- [73] S. Jia, Y. Su, B. Zhang, Z. Zhao, S. Li, Y. Zhang, P. Li, M. Xu, R. Ren, *Nanoscale* **2019**, *11*, 7690-7700.
- [74] a) J. Ma, J. Ren, Y. Jia, Z. Wu, L. Chen, N. O. Haugen, H. Huang, Y. Liu, *Nano Energy* **2019**, *62*, 376-383; b) Y. Zhang, X. Huang, J. Yeom, *Nano-Micro Lett.* **2019**, *11*, 11; c) D. Xiang, Z. Liu, M. Wu, H. Liu, X. Zhang, Z. Wang, Z. L. Wang, L. Li, *Small* **2020**, *16*, 1907603; d) J. Yuan, X. Huang, L. Zhang, F. Gao, R. Lei, C. Jiang, W. Feng, P. Liu, *Appl. Catal., B* **2020**, *278*, 119291.
- [75] a) X. Liu, L. Xiao, Y. Zhang, H. Sun, *J. Materiomics* **2020**, *6*, 256-262; b) S. Xu, Z. Liu, M. Zhang, L. Guo, *J. Alloys Compd.* **2019**, *801*, 483-488; c) H. Li, Y. Sang, S. Chang, X. Huang, Y. Zhang, R. Yang, H. Jiang, H. Liu, Z. L. Wang, *Nano Lett.* **2015**, *15*, 2372-2379; d) L. Guo, C. Zhong, J. Cao, Y. Hao, M. Lei, K. Bi, Q. Sun, Z. L. Wang, *Nano Energy* **2019**, *62*, 513-520.
- [76] a) Y. Zhao, Z.-B. Fang, W. Feng, K. Wang, X. Huang, P. Liu, *ChemCatChem* **2018**, *10*, 3397-3401; b) Y. Li, Q. Wang, H. Wang, J. Tian, H. Cui, *J. Colloid Interface Sci.* **2019**, *537*, 206-214.
- [77] B. Dai, C. Lu, J. Kou, Z. Xu, F. Wang, *J. Alloys Compd.* **2017**, *696*, 988-995.
- [78] W. Gu, W. Zhang, L. Zhu, W. Zou, H. Liu, Z. Fu, Y. Lu, *Mater. Lett.* **2019**, *241*, 115-118.
- [79] L. Qifeng, M. Jingjun, M. Sharma, R. Vaish, *J. Am. Ceram. Soc.* **2019**, *102*, 5807-5817.
- [80] a) B. Yang, C. Wu, J. Wang, J. Bian, L. Wang, M. Liu, Y. Du, Y. Yang, *Ceram. Int.* **2020**, *46*, 4248-4255; b) X.-Z. Deng, C. Song, Y.-L. Tong, G. Yuan, F. Gao, D.-Q. Liu, S.-T. Zhang, *PCCP* **2018**, *20*, 3648-3657.
- [81] Q. Fu, X. Wang, C. Li, Y. Sui, Y. Han, Z. Lv, B. Song, P. Xu, *RSC Adv.* **2016**, *6*, 108883-108887.
- [82] A. Al-Keisy, L. Ren, X. Xu, W. Hao, S. X. Dou, Y. Du, *J. Phys. Chem. C* **2019**, *123*, 517-525.
- [83] S. Joonwichien, E. Yamasue, H. Okumura, K. N. Ishihara, *RSC Adv.* **2011**, *1*, 1060-1063.
- [84] H. J. Huang, Y. H. Wang, Y.-F. C. Chau, H.-P. Chiang, J. C.-S. Wu, *Nanoscale Res. Lett.* **2019**, *14*, 323.
- [85] L. Shi, X. Wang, Y. Hu, Y. He, *Solar Energy* **2020**, *196*, 505-512.
- [86] C. Si, J. Zhou, H. Gao, G. Liu, *Adv. Powder Technol.* **2013**, *24*, 295-300.
- [87] Y. Lu, B. Ren, S. Chang, W. Mi, J. He, W. Wang, *Mater. Lett.* **2020**, *260*, 126979.
- [88] K. Zhang, S. Wang, Y. Yang, *Adv. Energy Mater.* **2017**, *7*, 1601852.
- [89] Y.-L. Liu, J. M. Wu, *Nano Energy* **2019**, *56*, 74-81.
- [90] a) S. Kumar, M. Sharma, A. Kumar, S. Powar, R. Vaish, *J. Ind. Eng. Chem.* **2019**, *77*, 355-364; b) X. Yu, S. Wang, X. Zhang, A. Qi, X. Qiao, Z. Liu, M. Wu, L. Li, Z. L. Wang, *Nano Energy* **2018**, *46*, 29-38.
- [91] Y. Feng, M. Xu, H. Liu, W. Li, H. Li, Z. Bian, *Nano Energy* **2020**, *73*, 104768.
- [92] K. Zhao, B. Ouyang, Y. Yang, *iScience* **2018**, *3*, 208-216.
- [93] W. Zhao, Q. Zhang, H. Wang, J. Rong, L. E. Y. Dai, *Nano Energy* **2020**, *104783*.

Entry for the Table of Contents



External fields, including the microwave, mechanical stress, temperature gradient, external electric field, magnetic field and the coupling of multiple fields, provide an effective and facile strategy to enhance the photocatalytic performance of semiconductors.